





Crossover from ordinary to higher order Van Hove singularity in a honeycomb system: A parquet renormalization group analysis

Yueh-Chen Lee ^{1,*}, Dmitry V. Chichinadze ^{2,†} and Andrey V. Chubukov ^{1,‡}

¹*School of Physics and Astronomy and William I. Fine Theoretical Physics Institute, University of Minnesota, Minneapolis, Minnesota 55455, USA*

²*National High Magnetic Field Laboratory, Tallahassee, Florida 32310, USA*

 (Received 22 January 2024; revised 14 March 2024; accepted 20 March 2024; published 4 April 2024)

We investigate the crossover from an ordinary Van Hove singularity (OVHS) to a higher order Van Hove singularity (HOVHS) in a model applicable to Bernal bilayer graphene and rhombohedral trilayer graphene in a displacement field. At small doping, these systems possess three spin-degenerate Fermi pockets near each Dirac point K and K' ; at larger doping, the three pockets merge into a single one. The transition is of Lifshitz type and includes Van Hove singularities. Depending on system parameters, there are either three separate OVHS or a single HOVHS. We model this behavior by a one-parameter dispersion relation, which interpolates between OVHS and HOVHS. In each case, the diverging density of states triggers various electronic orders (superconductivity, pair density wave, valley polarization, ferromagnetism, spin, and charge density wave). We apply parquet renormalization group (pRG) technique and analyze how the ordering tendencies evolve between OVHS and HOVHS. We report rich system behavior caused by disappearance/reemergence and pair production/annihilation of the fixed points of the pRG flow.

DOI: [10.1103/PhysRevB.109.155118](https://doi.org/10.1103/PhysRevB.109.155118)

I. INTRODUCTION

One of the key topics in the field of quantum materials is the interplay of different ordering tendencies for interacting electrons. Usually, the most interesting results come from regions of the phase diagram where multiple phases are nearby and compete for the place on the phase diagram. The well-known and well-studied examples are cuprates and Fe-pnictides/chalcogenides, in which the competitors are antiferromagnetism, superconductivity, pair-density-wave, charge density wave order (both real and current-type), and nematicity (see e.g., [1–3]). Some more recent examples of systems with multiple ordered states are twisted bilayer graphene (TBG) [4–10], Bernal bilayer graphene (BBG) [11,12], rhombohedral trilayer graphene (RTG) [13,14], and other hexagonal/honeycomb systems [15]. From theory perspective, the interplay between different ordering instabilities is a complex problem. In strongly correlated electron systems one has to rely on numerical methods and on a comparison of the energies of particular ordered states within, e.g., Hartree-Fock approximation (see e.g., [16,17]). For weakly/moderately correlated metallic systems, the competition can be analyzed in a controllable way if the polarizations in several different channels (particle-particle and particle-hole ones) are logarithmically singular. The examples are the interplay between superconductivity and magnetism in Fe-pnictides, where superconducting and antiferromagnetic polarizations are both logarithmic [18–20]

(superconducting because of Cooper logarithm and antiferromagnetic because of different signs of dispersion of fermions near a hole and an electron pocket), and the interplay between superconductivity and diagonal (Q, Q) charge order in the spin-fermion model for the cuprates, where both polarizations are again logarithmic [21–24].

When perturbation theory contains logarithms, one can attempt to sum up infinite perturbative series in $(g_i L)$, where g_i are the couplings and L is the logarithmic factor, and neglect terms that contain additional powers of g_i without logarithms. For the case when only a superconducting channel is logarithmic, this amounts to summing up Cooper logarithms and neglecting nonlogarithmic corrections. When there is more than one logarithmic channel, the computational procedure gets more involved as there are several “directions” in which perturbative series in $(g_i L)$ have to be extended. It turns out, however, that these series can be expressed as a set of coupled differential equations, known as parquet renormalization group (pRG) equations [25–27] (for a general review on parquet RG for metals, see [28,29]). By solving the coupled set of differential pRG equations and analyzing the pRG flow, one can identify the channel (particle-particle or particle-hole) in which the instability develops first. A conceptually similar approach, called functional RG (fRG) is to divide a Fermi surface into patches, instead of channels, and solve the set of coupled differential equations for the running couplings within patches (for a review, see [30], for fRG for RTG see [31]).

The RG analysis (both pRG and fRG) has been applied to fermions near a Lifshitz transition, in which its topology changes [32–38]. At the transition, the fermionic density of states diverges logarithmically, and polarizations in various channels become logarithmically singular. This divergence is

*lee02892@umn.edu

†chichinadze@magnet.fsu.edu

‡achubuko@umn.edu

known as Van Hove singularity [39]. The superconducting polarization generally diverges faster than other polarizations, as L^2 ; however, if there is a nesting, some particle-hole polarizations also diverge as L^2 . To treat the case of a nonperfect nesting, Furukawa, Rice, and Salmhofer [32] suggested treating $O(L)$ terms as L^2 terms with phenomenological prefactors, $\alpha_j < 1$. This way one can reduce logarithmic series to the set of differential equations with variable L^2 rather than L , solve them, and identify the leading instabilities. If the same instability wins in a sizable range of α_j , one can reasonably expect that this is the correct result, particularly because the leading instability develops at a finite $L \sim 1/\sqrt{g}$, when the difference between L^2 and L with a large prefactor is not crucial.

In recent years, several groups [40–45] extended the pRG analysis to higher order Van Hove singularity (HOVHS), in which the density of states diverges by a power law. Shtyk *et al.* argued [40] that by varying tight-binding parameters of several hexagonal/honeycomb systems, one can move from ordinary Van Hove singularity (OVHS) to HOVHS. For a HOVHS, superconducting channel is no longer special as the power-law divergent polarization in the particle-particle channel is comparable to polarizations in particle-hole channels. It has been proposed [40,42,45] that one can still write a set of pRG equations, keeping the same processes, which gave rise to a logarithmic flow of the couplings for an OVHS, and taking the derivative with respect to the power of a typical scale instead of its logarithm. This approach is less rigorous because the contributions from the processes, previously neglected as nonlogarithmic, are of the same order as the ones from formerly logarithmic processes. As a result, the one-to-one correspondence with the perturbation theory, which exists for pRG near an OVHS, is lost for a HOVHS. Still, a comparison between the solution of HOVHS pRG equations and the direct perturbation theory shows [42] that the difference is only quantitative and can be small numerically. This justifies, at least partly, the use of pRG for systems with HOVHS.

In this paper, we analyze the interplay between ordering tendencies near OVHS and HOVHS for a system of fermions on a honeycomb lattice. Specifically, we consider the model of low-energy fermions in the vicinity of two valleys, K and K' . Such an electronic configuration emerges in BBG and RTG in the presence of a finite displacement field [11–14]. The phase diagrams in OVHS and HOVHS limits are shown in Fig. 1. In both systems, electronic configuration at small hole/electron doping consists of three spin-degenerate small pockets near K and three near K' , while at larger doping there is one spin-degenerate Fermi surface near K and one near K' see Fig. 2(a). For noninteracting fermions, a topological transformation from three small pockets to one larger Fermi surface occurs via a Lifshitz-type transition and is accompanied by a Van Hove singularity. Depending on the strength of the displacement field, it can be an OVHS, where the three small pockets touch at three different k points, or a single HOVHS, in which case the DOS has a power-law singularity. As explained in Ref. [40], the case of HOVHS separates two qualitatively different OVHS: the one at which three small pockets merge at three Van Hove points at some critical doping, leading to two annular Fermi surfaces at larger doping, and the one at which another Fermi surface,

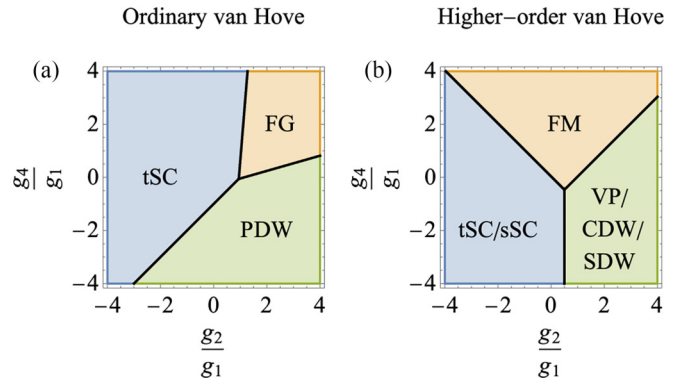


FIG. 1. The phase diagram in the OVHS limit (a) and HOVHS limit (b). The variables are the ratios of the bare couplings defined in Eq. (3). In the OVHS limit, the ordered states are spin-triplet superconductivity (tSC) and pair density wave (PDW), and there is a parameter range of asymptotically free Fermi gas with no order (FG). In the HOVHS limit, the ordered states are ferromagnetism (FM), superconductivity, degenerate between spin-triplet (tSC) and spin-singlet (sSC), and valley polarization (VP), degenerate with spin density wave (SDW) and charge density wave (CDW).

centered at $K(K')$, develops before the small pockets merge, and OVHS emerge where this new Fermi surface touches the three original pockets, see Fig. 3. The HOVHS emerges at the boundary separating two different types of OVHS, when three OVHS merge at one point [see Figs. 2(b), 2(c), and 3, and Ref. [40]]. A Van Hove singularity, which can be either ordinary or higher order, also emerges in the electronic spectrum in twisted bilayer WSe₂ either under a displacement field [46,47], or in the presence of Dzyaloshinskii-Moriya interaction [48].

For interacting fermions, the singularity in the density of states near an OVHS or an HOVHS gives rise to the emergence of electronic orders. We show that the ordering

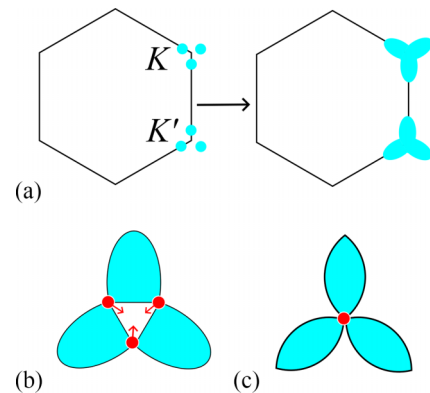


FIG. 2. (a) Band dispersion near K and K' points. At low doping (left), there are three smaller electron pockets (cyan circles) around K and three around K' . At high doping (right), the three pockets merge into a single Fermi surface. [(b),(c)] A zoomed-in sketch of the dispersion at the VH point in the OVHS case (b) and in the case of HOVHS (c). The red dots represent the VH points, and the arrows denote the direction in which they move throughout the crossover from OVHS to HOVHS. The dispersion at K' can be obtained by rotating (b) and (c) by 60 degrees.

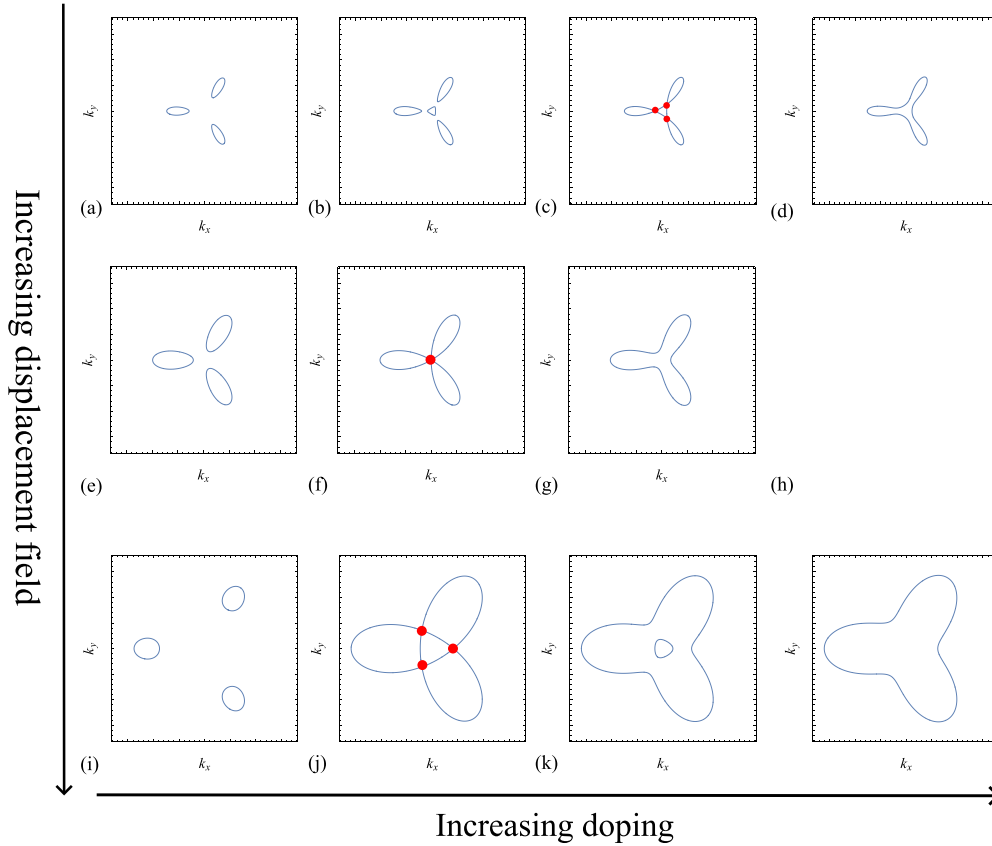


FIG. 3. The sketch of the three scenarios for the Fermi surface evolution between three small pockets near $K(K')$ and one larger pocket at $K(K')$, (three panels, depending on the strength of the displacement field). In each row, the doping increases from left to right, and Van Hove points are labeled as the red dots. In a weak displacement field (top panel), as doping increases, a new pocket emerges at $K(K')$, and at Van Hove doping, the three original pockets touch the center one, creating three OVHS. At larger doping, there is a singular Fermi surface. In a critical displacement field (middle panel), the three pockets touch each other at a single point, creating a HOVHS. In a strong displacement field (bottom panel) the three pockets increase upon doping and touch each other at Van Hove filling, creating again three OVHS. At larger doping, there are two annular Fermi surfaces.

tendencies for a system with OVHS significantly differ from those in a system with HOVHS (see Fig. 1). Specifically, for HOVHS, the ordered states, which develop in different parts of the phase diagram, are superconductivity, degenerate between spin-triplet and spin-singlet, and valley polarization, degenerate with spin and charge density waves [40,42,45]. For OVHS, the ordered states are spin-triplet superconductivity and pair-density wave. We analyze how the ordering tendencies evolve as the system is tuned from an OVHS towards a HOVHS.

To carry out this analysis, we consider a somewhat simplified model of the electronic dispersion, in which there is a single VHS at K and at K' , and tune the VHS between OVHS and HOVHS. Within such a model, the system can develop superconductivity, spin and valley polarizations, charge and spin-density wave orders with momenta $K - K' \equiv 2K$, and pair-density wave with the same momentum. In the full model with three pockets, these are the orders that preserve C_3 rotational symmetry between the pockets. The order that we cannot detect within our approximation, is nematic-like symmetry breaking between the three small pockets. Such symmetry breaking has been reported in the experiments on BBG [11,12,49]. The data, however, indicate that nematicity

develops only when there is a stronger spin or valley order of one of the types that we can detect within our model.

We model the dispersion by $\epsilon_k^{(\pm)} = \gamma k^2 \cos 2\theta \pm \sqrt{(1 - \gamma^2)k^3 \cos 3\theta}$, where the $+$ sign is K and $-$ for K' , k is the deviation from either K or K' , and θ is the angle with respect to, say k_x direction. We use γ as the tuning parameter. The limits $\gamma = 1$ and $\gamma = 0$ describe an OVHS and a HOVHS, respectively. In our analysis, we focus on the intermediate regime $\gamma \leq 1$, where the electronic dispersion has sizable contributions from both momentum-even ($k^2 \cos 2\theta$) and momentum-odd ($k^3 \cos 3\theta$) terms. We calculate the susceptibilities in different channels, derive and solve the pRG equations for the flow of the couplings, and determine how the leading and subleading ordering tendencies evolve as the system is tuned from OVHS to HOVHS. We find that the changes in the phase diagram are topological in nature and originate from multiple appearances and disappearances and pair production and annihilation of the fixed and saddle points of the RG flow.

II. THE MODEL AND ORDER PARAMETERS

We consider a system on a honeycomb lattice, consisting of two independent patches located at K and K' points in

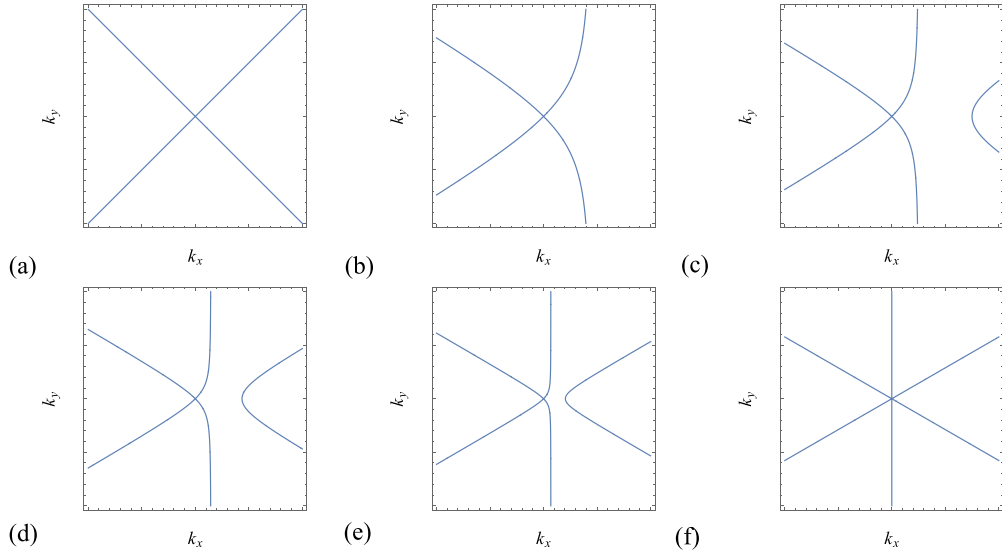


FIG. 4. The Fermi surface of Eq. (2) near the K' point (at $\epsilon_k^- = 0$) for (a) $\gamma = 1$, (b) $\gamma = 0.8$, (c) $\gamma = 0.6$, (d) $\gamma = 0.4$, (e) $\gamma = 0.2$, and (f) $\gamma = 0$. The Fermi surface at around K is the mirror image of the Fermi surface at K' .

the hexagonal Brillouin zone. We assume that at a given displacement field, the system is at critical doping, when there is a Van Hove singularity at the Fermi level. The free-fermion Hamiltonian is

$$H_2 = \sum_k (\epsilon_k^{(+)} c_{k+K}^\dagger c_{k+K} + \epsilon_k^{(-)} d_{k+K'}^\dagger d_{k+K'}), \quad (1)$$

where c and d operators correspond to fermions near the K and K' points, respectively, and k is the deviation from either K or K' . For an OVHS, the fermionic dispersion is around a Van Hove point, $\epsilon_k^{(\pm)}$, starts as k^2 , and is symmetric between K ($\epsilon_k^{(+)}$) and K' ($\epsilon_k^{(-)}$). For a HOVHS, the dispersion starts as k^3 and is antisymmetric between K and K' . We model the dispersion in the intermediate case by introducing a single tunable parameter γ ,

$$\epsilon_k^{(\pm)} = c_1 \gamma k^2 \cos 2\theta \pm c_2 \sqrt{(1-\gamma^2)} k^3 \cos 3\theta, \quad (2)$$

where θ is the angle with respect to, say k_x direction, and c_1, c_2 are constants, which we set to one below by rescaling the momentum k . We show the corresponding Fermi surface in Fig. 4. The dimensionless parameter γ varies in the range $0 \leq \gamma \leq 1$, where $\gamma = 1$ corresponds to OVHS and $\gamma = 0$ to HOVHS.

The full Hamiltonian includes four-fermion interactions, allowed by symmetry. A simple experimentation shows that there are three different interaction terms: interaction between fermionic densities within each valley, interaction between densities in different valleys, and intervalley exchange (Refs. [14,40,42,45,50,51])

$$H_4 = \sum_{k,k',q,q'} g_1 c_{k+K}^\dagger d_{q+K'} d_{k'+K'}^\dagger c_{q'+K} + g_2 c_{k+K}^\dagger c_{q+K} d_{k'+K'}^\dagger d_{q'+K'} + g_4 (c_{k+K}^\dagger c_{q+K} c_{k'+K}^\dagger c_{q'+K} + d_{k+K'}^\dagger d_{q+K'} d_{k'+K'}^\dagger d_{q'+K'}). \quad (3)$$

The momentum conservation in each term is implied ($k + k' = q + q'$). We use the same notations for the couplings

g_i with $i = 1, 2, 4$, as in [33,40]. The pair hopping interaction in the form $g_3 (c_{k+K}^\dagger c_{k'+K}^\dagger d_{q+K'} d_{q'+K'} + H.c.)$ is forbidden because $K - K' = 2K$ is not a reciprocal lattice vector. For generality, we do not assume a particular sign of the couplings, nor set the coupling g_1 for the exchange interaction with momentum transfer Q to be smaller than the couplings g_2 and g_4 for intrapocket and interpocket density-density interactions with small momentum transfer. The results for the BBG and RTG, in which $g_i > 0$ and $g_1 \ll g_2, g_4$, can be extracted from our generic phase diagrams below.

To study the ordering tendencies within the pRG, we introduce all possible order parameters involving fermions near K and K' . In the particle-hole channel, they are given by the expectation values of fermionic bilinears

$$\Delta = \langle f_{i,k}^\dagger T_{ij} S_{kl} f_{j,l} \rangle, \quad (4)$$

where $f_{i,j}$ are the fermion operators near K or K' . Here $i, j = 1, 2$ are spin indices, and T_{ij} is either a Kronecker delta δ_{ij} or a spin Pauli matrix $\vec{\sigma}_{ij}$ acting in spin space, while $k, l = 1, 2$ are valley indices, and S_{kl} is also either a Kronecker delta δ_{kl} or an isospin Pauli matrix $\vec{\sigma}_{kl}$ acting in the valley space. These order parameters can also be reexpressed in terms of the generators of $SU(4)$, as direct products of Pauli matrices acting in spin and valley spaces [51,52]. The total number of possible order parameters is 15; seven with zero momentum transfer and eight with momentum transfer $\pm Q$. The order parameters with zero momentum transfer are valley polarization $\Delta_{VP} = \langle d_\alpha^\dagger d_\alpha \rangle - \langle c_\alpha^\dagger c_\alpha \rangle$ and $3 \times 2 = 6$ intravalley ferromagnetic orders $\bar{\Delta}_{KM} = \langle c_\alpha^\dagger \vec{\sigma}_{\alpha,\beta} c_\beta \rangle$ and $\bar{\Delta}_{K'M} = \langle d_\alpha^\dagger \vec{\sigma}_{\alpha,\beta} d_\beta \rangle$. The latter two are coupled by g_1 , hence the global ferromagnetic and global antiferromagnetic orders $\bar{\Delta}_{KM} \pm \bar{\Delta}_{K'M}$ are competitors. The order parameters with momentum $\pm Q$ are two-complex charge density wave (CDW) $\Delta^{\text{CDW}}(\mathbf{Q}) = \langle c_\alpha^\dagger d_\alpha \rangle$, $\Delta^{\text{CDW}}(-\mathbf{Q}) = \langle d_\alpha^\dagger c_\alpha \rangle$ and $3 \times 2 = 6$ complex spin density wave (SDW) $\vec{\Delta}^{\text{SDW}}(\mathbf{Q}) = \langle c_\alpha^\dagger \vec{\sigma}_{\alpha,\beta} d_\beta \rangle$ and $\vec{\Delta}^{\text{SDW}}(-\mathbf{Q}) = \langle d_\alpha^\dagger \vec{\sigma}_{\alpha,\beta} c_\beta \rangle$.

TABLE I. Order parameters in particle-particle and particle-hole channels. The total number of order parameters is 19; 15 in the particle-hole channel and four in the particle-particle channel.

t/sSC	$\langle c_\alpha d_\beta \rangle \pm \langle c_\beta d_\alpha \rangle$
sPDW	$i\sigma_{\alpha\beta}^y \langle c_\alpha c_\beta \rangle; i\sigma_{\alpha\beta}^y \langle d_\alpha d_\beta \rangle$
r/iCDW	$\langle c_\alpha^\dagger \delta_{\alpha\beta} d_\beta \rangle \pm \langle d_\alpha^\dagger \delta_{\alpha\beta} c_\beta \rangle$
r/iSDW	$\langle c_\alpha^\dagger \bar{\sigma}_{\alpha\beta} d_\beta \rangle \pm \langle d_\alpha^\dagger \bar{\sigma}_{\alpha\beta} c_\beta \rangle$
VP	$\langle c_\alpha^\dagger c_\alpha \rangle - \langle d_\alpha^\dagger d_\alpha \rangle$
FM/AFM	$\langle c_\alpha^\dagger \bar{\sigma}_{\alpha\beta} c_\beta \rangle \pm \langle d_\alpha^\dagger \bar{\sigma}_{\alpha\beta} d_\beta \rangle$

In the particle-particle channel, we define $\Delta_{\alpha\beta}^{SC} = \langle c_\alpha^\dagger d_\beta^\dagger \rangle$ for Cooper pairs with zero total momentum and $\Delta_{\alpha\beta}^{K'PDW} = \langle c_\alpha^\dagger c_\beta^\dagger \rangle$ and $\Delta_{\alpha\beta}^{KPDW} = \langle d_\alpha^\dagger d_\beta^\dagger \rangle$ for pair density wave (PDW) with net momentum $\pm\mathbf{Q}$, where $\mathbf{Q} = \mathbf{K} - \mathbf{K}' \equiv 2\mathbf{K}$. The spin triplet/singlet superconducting order parameters can be obtained by adding/subtracting $\Delta_{\alpha\beta}^{SC}$ and $\Delta_{\alpha\beta}^{SC}$. The order parameters $\Delta_{\alpha\beta}^{SC}$ are coupled, hence spin-singlet/valley-triplet and spin-triplet/valley-singlet states are competitors. The two PDW order parameters $\Delta_{\alpha\beta}^{K'PDW}$ and $\Delta_{\alpha\beta}^{KPDW}$ are not coupled in the absence of pair hopping and develop simultaneously. Within our simplified model with a single Van Hove point at $K(K')$ and momentum-independent four-fermion interaction, only spin-singlet s -wave PDW is possible; the coupling for spin-triplet PDW vanishes. The total number of particle-particle order parameters is 4 ($\Delta_{\alpha\beta}^{SC}$, $\Delta_{\beta\alpha}^{SC}$, $\Delta_{\alpha\beta}^{K'PDW}$, $\Delta_{\alpha\beta}^{KPDW}$).

We present $4 + 15 = 19$ order parameters in Table I.

III. PHASE DIAGRAM IN THE TWO LIMITS

To set the stage for our pRG analysis, we first present the results in the two limiting cases of OVHS ($\gamma = 1$) and HOVHS ($\gamma = 0$). The phase diagram in the HOVHS limit has been previously obtained in [40,42,45]. The phase diagram in the OVHS limit has been obtained in [37]. Our phase diagram disagrees with theirs (see the next section for the reasoning).

The phase diagram in the two limits is presented in Fig. 1. Here and in subsequent figures we use the ratios of the bare couplings g_2/g_1 and g_4/g_1 as the two variables for the phase diagram.

In the OVHS case, there are three regions in the phase diagram. In the top right corner, all the couplings flow to zero, and the system asymptotically behaves like a free Fermi gas

(FG). In the rest of the phase diagram the leading instability is either s -wave pair-density-wave (PDW) or spin-triplet superconductivity (tSC).

In the HOVHS case, order develops for all ratios of g_2/g_1 and g_4/g_1 . There are three types of order, depending on the bare couplings: ferromagnetism (FM), superconductivity, degenerate between spin-triplet and spin-singlet (sSC), or valley polarization (VP) degenerate with spin-density-wave (SDW) and charge-density-wave (CDW).

We see that the ordered states are very different in the two cases. Our goal is to understand how the ordering tendency evolves as our tuning parameter γ changes between $\gamma = 0$ (OVHS) and $\gamma = 1$ (HOVHS). To address this, below we apply pRG procedure at varying γ .

IV. GENERAL PARQUET RG SCHEME

The general pRG scheme is the two-stage procedure [19,20,53,54]. In the first stage, one obtains and solves the set of coupled pRG equations for the coupling g_i . The renormalizations hold in both particle-particle and particle-hole channels, and can be graphically represented as running in two orthogonal directions (this is why the method is called ‘‘parquet’’ RG). In the second stage, one introduces infinitesimally small bare order parameters Δ_0^j and obtains and solves pRG equations for running Δ^j using the running couplings g_i as inputs. This allows one to obtain the corresponding susceptibilities. The strongest ordering tendency is for the order parameter with the largest susceptibility.

The pRG equations for g_i are expressed in terms of polarization bubbles—the fermionic loops in particle-particle and particle-hole channels. We start our discussion of the pRG flow by analyzing the polarization bubbles and their dependence on the parameter γ .

A. Polarization bubbles

Because in our simplified model the Van Hove points are located at K and K' relevant susceptibilities are at zero momentum and momentum $\mathbf{Q} = \mathbf{K} - \mathbf{K}'$. There are four relevant polarization bubbles $\Pi_{ph}(0)$, $\Pi_{ph}(\mathbf{Q})$, $\Pi_{pp}(0)$, and $\Pi_{pp}(\mathbf{Q})$. For our purposes, it is convenient to define all $\Pi_i(\mathbf{k})$ as positive. We have

$$\begin{aligned}
 \Pi_{ph}(0) &= -\frac{T}{(2\pi)^2} \sum_{\omega} \int \frac{d^2\mathbf{k}}{(i\omega - \epsilon_{\mathbf{k}}^+)^2} = -\frac{T}{(2\pi)^2} \sum_{\omega} \int \frac{d^2\mathbf{k}}{(i\omega - \epsilon_{\mathbf{k}}^-)^2}, \\
 \Pi_{ph}(\mathbf{Q}) &= -\frac{T}{(2\pi)^2} \sum_{\omega} \int \frac{d^2\mathbf{k}}{(i\omega - \epsilon_{\mathbf{k}}^+)(i\omega - \epsilon_{\mathbf{k}}^-)}, \\
 \Pi_{pp}(0) &= \frac{T}{(2\pi)^2} \sum_{\omega} \int \frac{d^2\mathbf{k}}{(i\omega - \epsilon_{\mathbf{k}}^+)(-i\omega - \epsilon_{-\mathbf{k}}^-)}, \\
 \Pi_{pp}(\mathbf{Q}) &= \frac{T}{(2\pi)^2} \sum_{\omega} \int \frac{d^2\mathbf{k}}{(i\omega - \epsilon_{\mathbf{k}}^+)(-i\omega - \epsilon_{-\mathbf{k}}^+)} = \frac{T}{(2\pi)^2} \sum_{\omega} \int \frac{d^2\mathbf{k}}{(i\omega - \epsilon_{\mathbf{k}}^-)(-i\omega - \epsilon_{-\mathbf{k}}^-)}.
 \end{aligned} \tag{5}$$

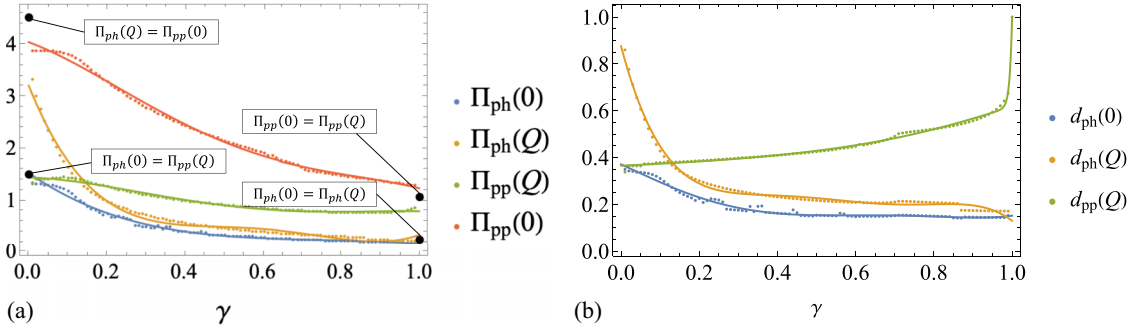


FIG. 5. (a) Polarization bubbles evaluated at $T = 10^{-4}$ as functions of γ —the control parameter for the crossover from OVHS to HOVHS ($\gamma = 1$ for OVHS and $\gamma = 0$ for HOVHS). (b) The polarizations normalized to $\Pi_{pp}(\mathbf{0})$, $d_i(\mathbf{k}) = \Pi_i(\mathbf{k})/\Pi_{pp}(\mathbf{0})$, which we used in the pRG equations. Scattered dots are the numerical results and solid curves are the fits to approximate analytical expressions (see Appendix D). Black dots, analytic results in the two limits, Eqs. (6) and (7).

Because the dispersion starts with k^2 , or even k^3 , the momentum integral is formally singular and has to be regularized. We use temperature regularization, i.e., evaluate the momentum integral at $q = 0$ or Q and a finite T , and set either $\log 1/T$ or $1/T^{1/3}$ (for HOVHS) as our pRG scale (see below). Evaluating the momentum integral at a finite T , we obtain in the OHVS limit ($\gamma = 1$)

$$\begin{aligned}\Pi_{ph}(\mathbf{Q}) = \Pi_{ph}(\mathbf{0}) &= \frac{1}{4\pi^2} \log(2.26/T), \\ \Pi_{pp}(\mathbf{Q}) = \Pi_{pp}(\mathbf{0}) &= \frac{1}{8\pi^2} \log^2(a/T), \quad a = O(1),\end{aligned}\quad (6)$$

and in the HOVHS limit ($\gamma = 0$)

$$\begin{aligned}\Pi_{ph}(\mathbf{Q}) = \Pi_{pp}(\mathbf{0}) &= 3X, \quad \Pi_{ph}(\mathbf{0}) = \Pi_{pp}(\mathbf{Q}) = X, \\ X &\approx \frac{0.07}{T^{1/3}}\end{aligned}\quad (7)$$

(see Appendices A and C for details). The authors of Ref. [37] evaluated the polarization bubbles $\Pi(q)$ at $q = 0$ and $q = Q$ right at $T = 0$ and obtained $\Pi_{ph}(\mathbf{0}) = 0$ because of the double pole. We believe that the polarization bubbles relevant to pRG have to be computed at a finite external energy scale. As a check, we computed the polarization bubbles $\Pi_{ph/pp}(q)$ at $T = 0$ but q different from 0 or Q and used q as the pRG parameter. We obtained the same results as with temperature regularization.

For $0 < \gamma < 1$, we evaluate polarization bubbles numerically at $T = 10^{-4}$. We present the results for the four Π 's in Fig. 5 as functions of γ . For convenience of calculations, we fitted the numerical results by analytical functions (solid lines in the fits) (see Appendix D). The use of scaling functions is advantageous as the ratios of polarization bubbles are given by ratios of analytic functions and can be easily evaluated without extensive numerical integration.

B. pRG equations

We see Fig. 5 that the intervalley particle-particle bubble $\Pi_{pp}(\mathbf{0})$ is the largest for all values of γ . It is then convenient to define $L = \Pi_{pp}(\mathbf{0})$ as our RG scale. That is define $\dot{g}_i = \frac{dg_i}{dL} = \frac{dg_i}{d\Pi_{pp}(\mathbf{0})}$. For other Π 's, we introduce the ratios $d_i(\mathbf{k}) = \frac{d\Pi_i(\mathbf{k})}{d\Pi_{pp}(\mathbf{0})}$.

For practical applications, increasing L amounts to lowering the temperature.

The one-loop pRG equations for the running g_i are obtained in a standard way, by evaluating one-loop diagrams for the renormalization of the four-fermion vertices, differentiating with respect to L , and replacing the bare internal vertices by the running ones, at the scale L . The equations are

$$\begin{aligned}\dot{g}_1 &= 2g_1(g_2 - g_1)d_{ph}(\mathbf{Q}) + 2g_1g_4d_{ph}(\mathbf{0}) - 2g_1g_2, \\ \dot{g}_2 &= g_2^2d_{ph}(\mathbf{Q}) + 2(g_1 - g_2)g_4d_{ph}(\mathbf{0}) - (g_1^2 + g_2^2), \\ \dot{g}_4 &= -g_4^2d_{pp}(\mathbf{Q}) + (g_1^2 + 2g_1g_2 - 2g_2^2 + g_4^2)d_{ph}(\mathbf{0}).\end{aligned}\quad (8)$$

The boundary condition is at $L = 0$, where the couplings are bare.

We see that the coupling g_1 is self-generated, i.e., $\dot{g}_1 = 0$ if $g_1 = 0$. For this reason, g_1 does not change sign under pRG. This property allows us to study the pRG flow in the space of $x_2 = g_2/g_1$ and $x_4 = g_4/g_1$. The equations for running x_2 and x_4 are

$$\begin{aligned}\dot{x}_2 &= g_1 \{ x_2^2 d_{ph}(\mathbf{Q}) + 2(1 - x_2)x_4 d_{ph}(\mathbf{0}) - (1 + x_2^2) \\ &\quad - x_2 [2(x_2 - 1)d_{ph}(\mathbf{Q}) + 2x_4 d_{ph}(\mathbf{0}) - 2x_2] \}, \\ \dot{x}_4 &= g_1 \{ -x_4^2 d_{pp}(\mathbf{Q}) + (1 + 2x_2 - 2x_2^2 + x_4^2)d_{ph}(\mathbf{0}) \\ &\quad - x_4 [2(x_2 - 1)d_{ph}(\mathbf{Q}) + 2x_4 d_{ph}(\mathbf{0}) - 2x_2] \}.\end{aligned}\quad (9)$$

As defined, $d_i(\mathbf{k})$ in Eqs. (8) and (9) are functions of L . The exception is the case of HOVHS ($\gamma = 0$), where all $\Pi_i(\mathbf{k})$ scale as $1/T^{1/3}$, and $d_i(\mathbf{k})$ are just numbers [$d\Pi_i(\mathbf{k})/d\Pi_{pp}(\mathbf{0}) = \Pi_i(\mathbf{k})/\Pi_{pp}(\mathbf{0})$]. Below we follow Refs. [29,32,33] and replace $d\Pi_i(\mathbf{k})/d\Pi_{pp}(\mathbf{0})$ by $\Pi_i(\mathbf{k})/\Pi_{pp}(\mathbf{0})$ for all values of γ . For the OHVS this amounts to replacing the ratios that scale as $1/\sqrt{L}$ by some small numbers from Fig. 5. We refer the reader to Refs. [29,32,33] for justification.

C. Fixed trajectories of pRG flow

In general, the pRG flow in the $x_2 - x_4$ plane is determined by the location of fixed trajectories, when all g_i either diverge or vanish, but the ratios of the couplings tends to finite values. In terms of $x_2 = g_2/g_1$ and $x_4 = g_4/g_1$, which we will be using, these fixed trajectories are fixed points, satisfying $\dot{x}_2 = 0$ and $\dot{x}_4 = 0$. There are three generic possibilities for

fixed points: a stable fixed point, an unstable fixed point, and a saddle point (half-stable fixed point). The stability of a fixed point is determined by the eigenvalues of the matrix

$$\begin{pmatrix} d\dot{x}_2/dx_2 & d\dot{x}_2/dx_4 \\ d\dot{x}_4/dx_2 & d\dot{x}_4/dx_4 \end{pmatrix}. \quad (10)$$

A stable fixed point has two negative eigenvalues, an unstable fixed point has two positive eigenvalues, and a half-stable fixed point has one positive and one negative eigenvalue.

We label the fixed points in the (x_2, x_4) plane as (c_2, c_4) . Substituting $g_2 = c_2 g_1$ and $g_4 = c_4 g_1$ into Eq. (8), we obtain three equations in the form

$$\dot{g}_1 = f_i(c_2, c_4)g_1^2, \quad i = 1, 2, 4. \quad (11)$$

The set of equations $f_1(c_2, c_4) = f_2(c_2, c_4) = f_4(c_2, c_4)$ determines the values c_2 and c_4 . Then, if $f_i(c_2, c_4) > 0$, all the couplings diverge upon pRG at some scale L_0 , where the temperature corresponding to L_0 defines the critical temperature. Near $L = L_0$, $g_i \sim 1/(L_0 - L)$. If $f_i(c_2, c_4) < 0$, all the couplings tend to zero under pRG.

Besides fixed points, there can be also fixed lines on the (x_2, x_4) plane, specified by $x_4 = \xi x_2$. Such lines define the asymptotic direction or pRG flow at $x_2, x_4 \rightarrow \pm\infty$, i.e., when the magnitude of g_2 and g_4 becomes parametrically larger than g_1 . The slope ξ can be obtained by substituting $\dot{x}_4 = \xi \dot{x}_2$ into Eq. (9) and taking the limit $|x_2|, |x_4| \rightarrow \infty$. We find

$$\xi = \frac{d_{ph}(\mathbf{Q}) - 1 \pm \sqrt{24d_{ph}(0)^2 + (d_{ph}(\mathbf{Q}) - 1)^2 - 8d_{ph}(0)d_{pp}(\mathbf{Q})}}{6d_{ph}(0) - 2d_{pp}(\mathbf{Q})}.$$

D. The flow of the order parameters

The candidate order parameters Δ^i are listed in Sec. II. The generic equation for the flow of Δ^i is [19,53]

$$\dot{\Delta}^i = \lambda_i \Delta^i, \quad (12)$$

where the couplings $\lambda_i = d_i(\mathbf{k})g_i$ are linear combinations of the products of g_1, g_2 , and g_4 and the ratios of the polarization bubbles. These couplings can be obtained by solving ladder equations for the order parameters [50]. At the boundary, Δ_0^i is an infinitesimally small bare order parameter. An instability towards a finite Δ^i occurs when one or more couplings g_i diverge as $g_i \sim 1/(L_0 - L)$. The order parameter Δ_i then generally diverges as

$$\Delta^i \sim \frac{\Delta_0^i}{(L_0 - L)^{\beta_i}}.$$

The corresponding susceptibility χ_i is obtained by solving $\frac{d\chi_i}{dL} = \Delta^2$ (Refs. [19,53]) and scales as $\chi_i \sim \frac{1}{(L_0 - L)^{2\beta_i - 1}}$. The leading instability is determined by the largest critical exponent β_i .

In the particle-particle channel, the order parameters with momentum $q = 0$ satisfy [50]

$$\dot{\Delta}^{SC} = g_2 \Delta^{SC} + g_1 (\Delta^{SC})^*. \quad (13)$$

By adding/subtracting the equations for $\dot{\Delta}^{SC}$ and its complex conjugate, we find the couplings in the sSC / tSC channels are

$$\lambda_{t/sSC} = -(g_2 \mp g_1).$$

For PDW, we have

$$\dot{\Delta}^{PDW} = g_4 d_{pp}(Q) \Delta^{PDW}. \quad (14)$$

The equation is the same for PDW with $2K$ and $2K'$. In the particle-hole channel the test order parameter vertices satisfy

[50,55]

$$\begin{aligned} \dot{\Delta}^{SDW}(\mathbf{Q}) &= d_{ph}(\mathbf{Q})g_2 \Delta^{SDW}(\mathbf{Q}), \\ \dot{\Delta}^{SDW}(-\mathbf{Q}) &= d_{ph}(\mathbf{Q})g_2 \Delta^{SDW}(-\mathbf{Q}), \\ \dot{\Delta}^{CDW}(\mathbf{Q}) &= d_{ph}(\mathbf{Q})(g_2 - 2g_1) \Delta^{CDW}(\mathbf{Q}), \\ \dot{\Delta}^{CDW}(-\mathbf{Q}) &= d_{ph}(\mathbf{Q})(g_2 - 2g_1) \Delta^{CDW}(-\mathbf{Q}), \\ \dot{\Delta}^{VP} &= d_{ph}(0)(2g_2 - g_1 - g_4) \Delta^{VP}, \\ \dot{\Delta}^{KM} &= d_{ph}(0)(g_4 \Delta^{KM} + g_1 \Delta^{K'M}), \\ \dot{\Delta}^{K'M} &= d_{ph}(0)(g_4 \Delta^{K'M} + g_1 \Delta^{KM}). \end{aligned} \quad (15)$$

We then obtain

$$\begin{aligned} \lambda^{CDW}(\mathbf{Q}) &= \lambda^{CDW}(-\mathbf{Q}) = d_{ph}(\mathbf{Q})(g_2 - 2g_1), \\ \lambda^{SDW}(\mathbf{Q}) &= \lambda^{SDW}(-\mathbf{Q}) = d_{ph}(\mathbf{Q})g_2. \end{aligned}$$

The coupling constants for SDW and CDW order parameters at momentum transfer \mathbf{Q} are the same as for those at $-\mathbf{Q}$. This just reflects the two-component nature of CDW and SDW order parameters.

Further,

$$\lambda_{VP} = d_{ph}(0)(2g_2 - g_4 - g_1),$$

and

$$\lambda_{FM/AFM} = d_{ph}(0)(g_4 \pm g_1),$$

for the couplings of global ferromagnetism and global antiferromagnetism. We list the couplings in Table II.

V. RESULTS

We solved the pRG equations for the running couplings g_i for arbitrary γ between 0 and 1, used g_i to obtain susceptibilities for various order parameters, found the largest exponent λ_i and identified the leading ordering tendencies for various x_2 and x_4 .

We first present the results and discuss how we obtained them below and in Appendix E. The behavior at $\gamma = 1$ and

TABLE II. The couplings for various order parameters in terms of running g_i . An order parameter may develop only when the corresponding coupling is positive.

t/sSC	$-(g_2 \mp g_1)$
sPDW	$-d_{pp}(\mathbf{Q})g_4$
CDW	$d_{ph}(\mathbf{Q})(g_2 - 2g_1)$
SDW	$d_{ph}(\mathbf{Q})g_2$
VP	$d_{ph}(0)(-g_4 - g_1 + 2g_2)$
FM/AFM	$d_{ph}(0)(g_4 \pm g_1)$

$\gamma = 0$ is shown in Fig. 1. We show the evolution of the phase diagram with γ in Fig. 6. Each modification of the phase diagram develops at a particular γ , listed in the figure. We see that the evolution starts at γ very close to 1, i.e., already a small deviation from the OVHS changes the phase diagram and ordering tendencies. Another change of the ordering tendencies happens at γ near $0.1 \sim 0.2$. Comparing with Fig. 5(b), we see that the first change is caused by rapid drop of $d_{pp}(\mathbf{Q})$, while the second is caused by crossing of $d_{pp}(\mathbf{Q})$ and $d_{ph}(\mathbf{Q})$.

In practical terms, as γ decreases from 1, first the boundary between tSC and PDW states rotates until it becomes vertical, and simultaneously the FG region is replaced by tSC order. Next, the PDW order is replaced by the VP order. Then susceptibilities for tSC and sSC become degenerate. At even smaller γ , the FM phase is created at the top of the phase diagram. Finally, at $\gamma = 0^+$, the VP phase in the bottom right corner becomes degenerate with CDW and SDW.

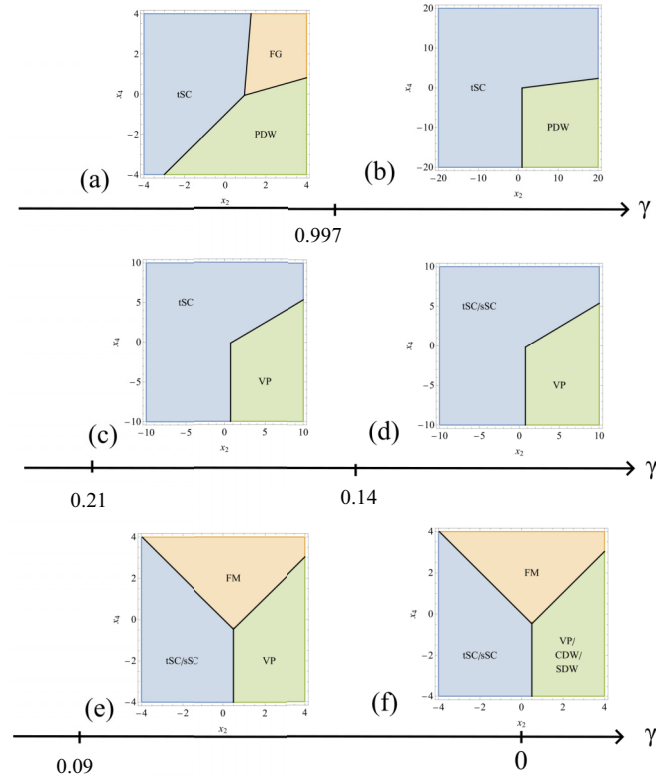


FIG. 6. The evolution of the phase diagram between OVHS and HOVHS. We describe the evolution in the text.

We now show the flow of the couplings, from which the evolution of the phase diagram has been extracted. We will see that the crossover between OVHS and HOVHS involves the disappearance and emergence of fixed points of the RG flow via (i) fixed points approaching infinity and (ii) pair creation or annihilation of fixed points.

We display the evolution of the flow in various panels in Fig. 7. For $\gamma = 1$ [panel (a)], there is a stable fixed point P_1 , an unstable fixed point P_2 , and two half-stable fixed points P_3 and P_4 . Once γ decreases, the half-stable fixed point P_3 quickly moves towards the lower left corner [panel (b)] and at $\gamma = 0.9984$ reaches $(-\infty, -\infty)$ [panel (c)]. At infinitesimally smaller γ , P_3 reemerges at $(+\infty, +\infty)$, now as a stable fixed point [panel (d)] (the positive eigenvalue changes sign and becomes negative). For simplicity, we keep the same notation P_3 for the re-emerging fixed point; this does not imply that the re-emerged fixed point describes the same ordered state as the one that disappears. At $\gamma = 0.997$, the fixed points P_3 and P_4 annihilate [panel (e)]. We show how this happens in more detail in Fig. 13 in Appendix E. After annihilation, the pRG flow everywhere in the upper part of the phase diagram is towards the stable fixed point P_1 [panel (f)]. Next, at smaller γ , the stable fixed point P_1 starts moving towards $(-\infty, -\infty)$ [panel (g)]. It reaches $(-\infty, -\infty)$ at $\gamma = 0.14$ [panel (h)], reappears at $(+\infty, +\infty)$ as a half-stable fixed point (one of the eigenvalues becomes positive, another remains negative), and starts moving towards the unstable point P_2 [panel (i)]. After that, the pRG flow in the left part of the phase diagram is towards $(-\infty, -\infty)$. In this flow, g_2 becomes parametrically larger than g_1 , which leads to degeneracy between sSC and tSC (see Table II). At even smaller γ , a pair of fixed points P_5 and P_6 is created at $\gamma = 0.09$ [panel (j)], and starts moving apart [panel (k)]. After that, the structure of fixed points becomes the same as in the limit of HOVHS [panel (l)].

The evolution of the fixed points gives rise to the evolution of the ordering tendencies. The leading ordering tendency, the one with the largest coupling λ_i , is displayed by the corresponding color in the phase diagram in Fig. 7. The computation of λ_i based on the pRG results for g_i is straightforward. We discuss the details in Appendix E and here show, as an example, the flow of the couplings λ_i in various channels in the OVHS limit, $\gamma = 1$ (Fig. 8) and in the HOVHS limit, $\gamma = 0$ (Fig. 9).

Application to BBG and RTG

For practical applications to BBG and RTG, we use the fact that bare couplings g_2 and g_4 are positive and nearly equal and are larger than bare g_1 , as g_2 and g_4 are the interactions with near-zero momentum transfer, while g_1 is the interaction with momentum transfer $2K$. The corresponding points on the phase diagram are near the diagonal in the upper-right quadrant (we show an example of pRG flow at large initial x_2 and x_4 in Fig. 10). We see from the phase diagram in Fig. 1 that for OVHS, the system is not ordered, while in the case of HOVHS, the order is ferromagnetic, and there is a wide intermediate regime, where the ordered state is a triplet superconductor. The reason why there is no order in the OVHS limit is due to the strongest effect from the renormalization in the particle-particle channel, which for positive (repulsive) inter-

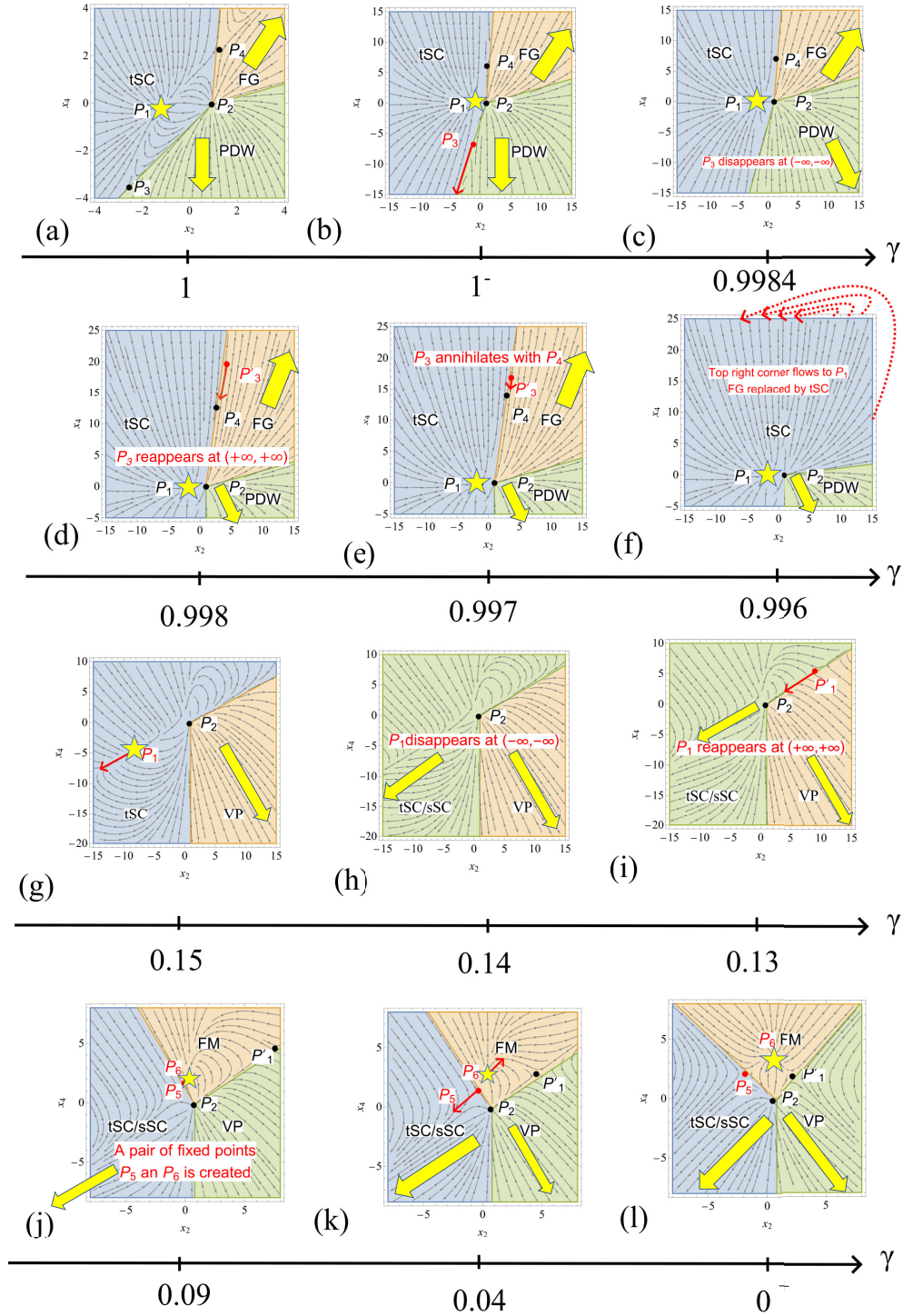


FIG. 7. Evolution of the pRG flow when γ becomes smaller than 1. Red arrows denote the movements of the fixed points. The stable fixed points and fixed lines are marked by yellow stars and yellow arrows.

actions drives g_i to zero. In the HOVHS limit, ferromagnetism is the consequence of the fact that the diagonal direction in the upper-right quadrant is in the basin of attraction of the fixed point P_6 in Fig. 7(l). This fixed point is at $x_4 \gg x_2$ i.e., the dressed g_4 is much larger than dressed x_2 . In this case, the ordered state is a FM (see Table II). At intermediate γ , the pRG flow in the upper-right corner of the phase diagram

is either towards the fixed point P_1 in Fig. 7(f), or towards $(-\infty, -\infty)$. In both cases, x_2 and x_4 become negative, which results in either tSC (flow towards P_1) or tSC degenerate with sSC [flow towards $(-\infty, -\infty)$]. We also emphasize that to get an instability towards FM one has to keep g_1 in the pRG equations. It is small initially, but grows under pRG and eventually determines the pRG flow of the other two couplings g_2

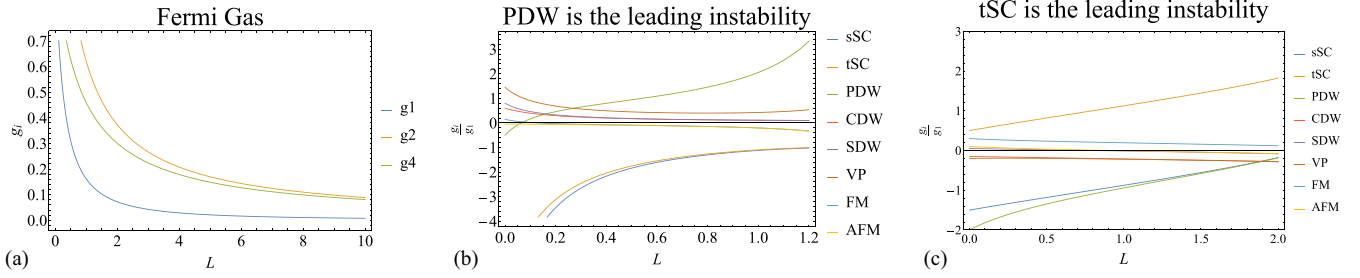


FIG. 8. The pRG flow as a function of L in the OHVS limit for the bare values (a) $x_2^0 = 2$, $x_4^0 = 1$, (b) $x_2^0 = 8$, $x_4^0 = 0.5$, and (c) $x_2^0 = 0.5$ and $x_4^0 = 2$.

and g_4 . Indeed, using $d_{ph}(0) = d_{pp}(\mathbf{Q}) = 1/3$ and $d_{ph}(Q) = 1$ at HOVHS, we obtain from (8)

$$\begin{aligned}\dot{g}_1 &= \frac{2}{3}g_1g_4 - 2g_1^2, \\ \dot{g}_2 &= \frac{2}{3}(g_1 - g_2)g_4 - g_2^2, \\ \dot{g}_4 &= \frac{2}{3}g_2(g_1 - g_2) + \frac{1}{3}g_1^2.\end{aligned}\quad (16)$$

If we neglected g_1 , we would find that g_2 and g_4 flow to zero. However, for a nonzero positive bare g_i , the couplings flow towards the fixed trajectory at $x_4 = g_4/g_1 = (3 + 2\sqrt{3})/2$ and $x_2 = g_2/g_1 = 1/2$, and the overall flow $\dot{g}_1 = g_1^2/(3 + 2\sqrt{3})$ is towards strong coupling, i.e., towards an ordered state. This fixed trajectory [fixed point on (x_2, x_4) plane] is P_6 in Fig. 7(l). Along the same lines one can also verify the flow of x_4 and x_2 at intermediate γ from initially large positive values towards the tSC fixed point P_1 [Fig. 7(f)] or towards $(-\infty, -\infty)$ [Fig. 7(h)]. In both cases, the initially repulsive pairing interactions becomes attractive in the process of the pRG flow.

VI. DISCUSSION AND CONCLUSIONS

The purpose of this study was to investigate leading ordering tendencies in a system of interacting fermions on a honeycomb lattice, which, upon doping, undergoes a Lifshitz-type transition from small pockets to a single Fermi surface via Van Hove singularity. Such a behavior has been detected in Bernal bilayer graphene and rhombohedral trilayer graphene under the displacement field [11–14]. Our main goal was to analyze the evolution of the ordering tendencies upon the change of fermionic dispersion under which there is a

transformation from an OVHS, with logarithmic divergence of the density of states, to HOVHS, when the density of states diverges by a power law. To address this issue, we introduced a toy model with Van Hove points at K and K' points in the Brillouin zone. The dispersion around Van Hove points is governed by a single parameter γ , by changing which one can tune from OVHS ($\gamma = 1$) to HOVHS ($\gamma = 0$).

To study the phase diagram of the system and its evolution between OVHS and HOVHS, we employed the pRG approach. We found that phase diagrams at $\gamma = 0$ and $\gamma = 1$ differ significantly. In the OVHS limit the two possible ordered phases are triplet superconductivity, s -wave pair-density wave state, and there is a region in the phase diagram with no order. In the HOVHS limit, the superconducting phase still exists, but spin-triplet and spin-singlet states are degenerate. Other orders that develop for different bare values of the interactions are ferromagnetism and valley polarization, degenerate with spin and charge density wave.

We applied the pRG procedure to γ between zero and one and found that the evolution between the two limits is a multi-stage process with severe changes in the structure of the pRG flow due to the annihilation and recreation of individual fixed points, once they reach the boundary of the phase diagram at infinity, and annihilation and creation of pairs of fixed points within the phase diagram. In terms of the ordered states, as γ decreases from one, first the Fermi gas phase is replaced by spin-triplet superconductivity, then PDW order loses to valley polarization, then spin-singlet superconducting state becomes attractive and degenerate with spin-triplet state, then a part of superconducting region becomes a ferromagnet, and, finally, spin/charge density wave channels become attractive and at $\gamma = 0^+$ become degenerate with valley polarization.

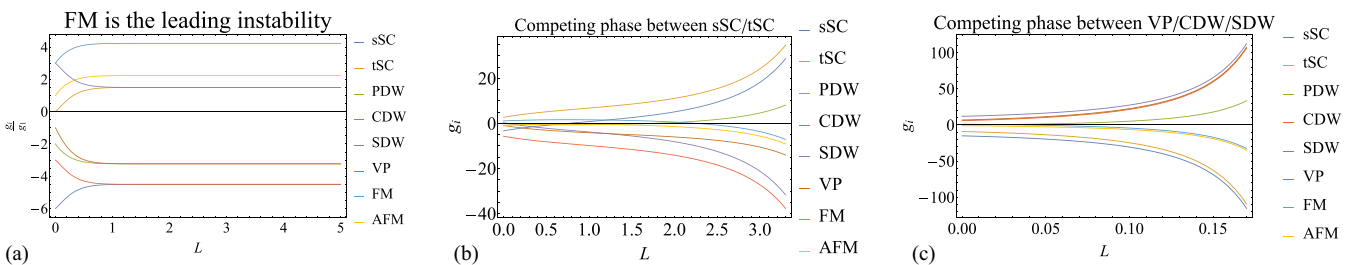


FIG. 9. The pRG flow as a function of L in the HOVHS limit for the bare values (a) $x_2^0 = 1$, $x_4^0 = 2$, (b) $x_2^0 = 0.1$, $x_4^0 = 0.1$, and (c) $x_2^0 = 4$, $x_4^0 = 0.1$.

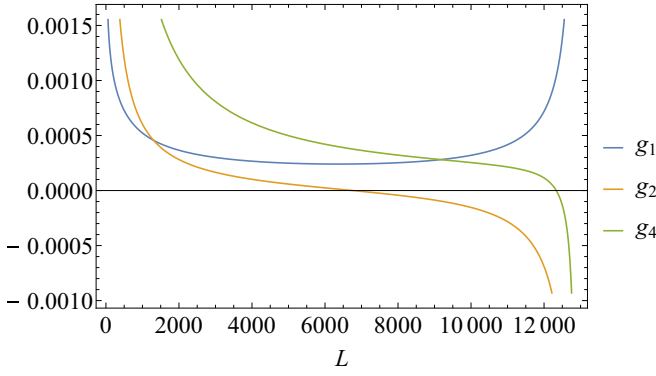


FIG. 10. The pRG flow of the couplings with $x_2^0 = x_4^0 = 100$ at $\gamma = 0.9$.

All ordered states develop at a finite energy. In this regard, our results show how different orders compete and replace each other as the fermionic dispersion is modified at a finite energy offset from the Van Hove singularity. This offset provides a scale that separates the region where the effects of higher order Van Hove singularity become important from the region where they are negligible. We expect our results to be applicable, besides BBG and RTG, to a number of twisted and untwisted systems, which undergo Lifshitz-type transition upon doping [56–59], e.g., to twisted WSe₂ under displacement field [60,61].

ACKNOWLEDGMENTS

The authors acknowledge with thanks useful discussions with L. Classen, R. Fernandes, Y. Huang, Y.-P. Lin, K. R. Islam, R. D. Mayrhofer, L. Santos, D. Shaffer, and B. Shklovskii. The work by Y.-C.L. and A.V.C. was supported by the U.S. Department of Energy, Office of Science, Basic Energy Sciences, under Award No. DE-SC0014402. D.V.C. acknowledges financial support from the National High Magnetic Field Laboratory through a Dirac Fellowship, which is funded by the National Science Foundation (Grant No. DMR-1644779) and the State of Florida.

APPENDIX A: CALCULATION OF POLARIZATION OPERATORS IN THE HOVHS LIMIT

In the HOVHS limit, $\gamma = 0$, the dispersion for two patches is given by

$$\varepsilon_{\mathbf{k}}^{\pm} = \pm k^3 \cos 3\theta,$$

where indices \pm labels valleys (patches). We will use temperature as a regularizer.

Like we said in the main text, we use the sign convention in which all polarization bubbles are positive. Following (5) and using

$$\varepsilon_{\mathbf{k}}^+ = -\varepsilon_{-\mathbf{k}}^-, \quad \varepsilon_{-\mathbf{k}}^+ = -\varepsilon_{\mathbf{k}}^+$$

we have

$$\begin{aligned} \Pi_{ph}(0) &= -T \sum_{\omega} \int \frac{d^2k}{4\pi^2} \frac{1}{(i\omega - \varepsilon_{\mathbf{k}}^+)^2} = I_1, \\ \Pi_{ph}(Q) &= -T \sum_{\omega} \int \frac{d^2k}{4\pi^2} \frac{1}{(i\omega - \varepsilon_{\mathbf{k}}^+)(i\omega + \varepsilon_{\mathbf{k}}^+)} = I_2, \\ \Pi_{pp}(0) &= T \sum_{\omega} \int \frac{d^2k}{4\pi^2} \frac{1}{(i\omega - \varepsilon_{\mathbf{k}}^+)(-i\omega - \varepsilon_{\mathbf{k}}^+)} = I_2, \\ \Pi_{pp}(Q) &= T \sum_{\omega} \int \frac{d^2k}{4\pi^2} \frac{1}{(i\omega - \varepsilon_{\mathbf{k}}^+)(-i\omega + \varepsilon_{\mathbf{k}}^+)} = I_1, \end{aligned} \quad (\text{A1})$$

where I_1 and I_2 are the two integrals that need to be calculated,

$$I_1 = \frac{1}{16\pi^2 T} \int \frac{d^2k}{\cosh^2 \frac{\varepsilon_{\mathbf{k}}^+}{2T}}, \quad I_2 = \frac{1}{8\pi^2} \int \frac{d^2k \tanh \frac{\varepsilon_{\mathbf{k}}^+}{2T}}{\varepsilon_{\mathbf{k}}^+}.$$

1. Calculation of I_1

Consider I_1 first. There the integral can be taken by performing an appropriate change of variables,

$$\begin{aligned} I_1 &= \frac{1}{16\pi^2 T} \int \frac{d^2k}{\cosh^2 \frac{\varepsilon_{\mathbf{k}}^+}{2T}} \\ &= \frac{3(2T)^{2/3}}{16\pi^2 T} \int_{-\pi/6}^{\pi/6} \frac{d\theta}{(\cos 3\theta)^{2/3}} \int \frac{d(k^2 (\cos 3\theta)^{2/3} / (2T)^{2/3})}{\cosh^2 \frac{k^3 \cos 3\theta}{2T}} \\ &= \frac{3 \cdot 2^{2/3}}{4T^{1/3} (2\pi)^2} \int_{-\pi/6}^{\pi/6} \frac{d\theta}{(\cos 3\theta)^{2/3}} \int_0^{\infty} \frac{dx}{\cosh^2 x^{3/2}}. \end{aligned} \quad (\text{A2})$$

Note, that we can set the upper limit of the x integration to infinity as the integral is convergent; the integral over θ is convergent as well. Using

$$\begin{aligned} \int_0^{\infty} \frac{dx}{\cosh^2 x^{3/2}} &\simeq 0.958, \\ \int_{-\pi/6}^{\pi/6} \frac{d\theta}{(\cos 3\theta)^{2/3}} &\simeq 2.43 \end{aligned} \quad (\text{A3})$$

we obtain the final result

$$I_1 \simeq 0.07T^{-1/3}. \quad (\text{A4})$$

We can also do an approximate calculation using Taylor-expanded dispersion near the points where $\cos 3\theta = 0$; such calculations will prove useful in the intermediate regime. Expanding near $\theta = \pi/6$ and multiplying by 6 to accommodate for all lines of zero energy, we obtain the approximate expression

$$\begin{aligned} I_1 &\simeq \frac{1}{4T(2\pi)^2} \int \frac{d^2k}{\cosh^2 \frac{\varepsilon_{\mathbf{k}}^+}{2T}} \simeq \frac{6}{4T(2\pi)^2} \int \frac{k dk d\theta}{\cosh^2 \frac{3k^3\theta}{2T}} \\ &= \frac{3^{1/3}}{2(2T)^{1/3}(2\pi)^2} \int_0^1 \frac{d\theta}{\theta^{2/3}} \int_0^{\infty} \frac{d\left(\frac{3^{2/3}k^2\theta^{2/3}}{2T}\right)}{\cosh^2 \frac{3k^3\theta}{2T}} \\ &= \frac{3^{1/3}}{2(2T)^{1/3}(2\pi)^2} \int_0^1 \frac{d\theta}{\theta^{2/3}} \int_0^{\infty} \frac{dx}{\cosh^2 x^{3/2}}. \end{aligned} \quad (\text{A5})$$

Hence, we get for I_1

$$I_1 \simeq \frac{3^{1/3}}{2(2T)^{1/3}(2\pi)^2} \times 3 \times 0.958 = 0.042T^{-1/3}. \quad (\text{A6})$$

This approximate result is about 0.6 of the exact expression.

One can also calculate the same integral without taking into account the angular dependence of the dispersion. In this case $\varepsilon = k^3$. The analog of I_1 , which we define as I_1^* , is

$$\begin{aligned} I_1^* &= \frac{1}{4T(2\pi)^2} \int \frac{d^2k}{\cosh^2 \frac{\varepsilon_k}{2T}} = \frac{1}{4T(2\pi)^2} \int \frac{kdkd\theta}{\cosh^2 \frac{k^3}{2T}} \\ &= \frac{1}{4(2T)^{1/3}(2\pi)} \int_0^\infty \frac{d\left(\frac{k^2}{(2T)^{2/3}}\right)}{\cosh^2 \frac{k^3}{2T}} \\ &= \frac{1}{4(2T)^{1/3}(2\pi)} \int_0^\infty \frac{dx}{\cosh^2 x^{3/2}} \simeq 0.03T^{-1/3}. \quad (\text{A7}) \end{aligned}$$

2. Calculation of I_2

Now consider I_2 . We perform the same change of variables to obtain

$$\begin{aligned} I_2 &= \frac{1}{2(2\pi)^2} \int \frac{d^2k \tanh \frac{\varepsilon_k}{2T}}{\varepsilon_k^+} = \frac{3(2T)^{2/3}}{2(2\pi)^2(2T)} \\ &\cdot \int_{-\pi/6}^{\pi/6} \frac{d\theta}{(\cos 3\theta)^{2/3}} \int \frac{\left(\frac{\cos 3\theta}{2T}\right)^{2/3} dk^2}{k^3 \cos 3\theta / 2T} \tanh \frac{k^3 \cos 3\theta}{2T} \\ &= \frac{3(2T)^{2/3}}{2(2\pi)^2(2T)} \int_{-\pi/6}^{\pi/6} \frac{d\theta}{(\cos 3\theta)^{2/3}} \int_0^\infty \frac{dx}{x^{3/2}} \tanh x^{3/2}. \quad (\text{A8}) \end{aligned}$$

The integral over x yields

$$\int_0^\infty \frac{dx \tanh x^{3/2}}{x^{3/2}} = 3 \int_0^\infty \frac{dx}{\cosh^2 x^{3/2}} \simeq 2.87, \quad (\text{A9})$$

as can be verified by integration by parts. Therefore,

$$I_2 = 3I_1 \simeq 0.21T^{-1/3}. \quad (\text{A10})$$

A similar approximate calculation can be done here as well. Expanding near $\theta \simeq \pi/6$, multiplying by six contributions from six angles where $\cos 3\theta = 0$, we obtain

$$\begin{aligned} I_2 &\simeq \frac{6}{2(2\pi)^2} \int \frac{kdkd\theta \tanh \frac{3k^3\theta}{2T}}{3k^3\theta} \\ &= \frac{3^{1/3}}{2(2\pi)^2(2T)^{1/3}} \int_0^1 \frac{d\theta}{\theta^{2/3}} \int \frac{d\left(\frac{3^{2/3}k^2\theta^{2/3}}{(2T)^{2/3}}\right) \tanh \frac{3k^3\theta}{2T}}{3k^3\theta/2T} \\ &= \frac{3^{1/3}}{2(2\pi)^2(2T)^{1/3}} \int_0^1 \frac{d\theta}{\theta^{2/3}} \int_0^\infty \frac{dx \tanh x^{3/2}}{x^{3/2}}. \quad (\text{A11}) \end{aligned}$$

Evaluating the last integral, we obtain

$$I_2 \simeq \frac{3^{1/3}}{2(2\pi)^2(2T)^{1/3}} \times 3 \times 2.87T^{-1/3} \simeq 0.126T^{-1/3}. \quad (\text{A12})$$

Evidently, I_1 and I_2 differ by a factor of 3.

One can also calculate I_2 for the cubic dispersion without the angular dependence, i.e., $\varepsilon = k^3$. The analog of I_2 ,

which we define as I_2^* , is

$$\begin{aligned} I_2^* &= \frac{1}{2(2\pi)^2} \int \frac{kdkd\theta \tanh \frac{k^3}{2T}}{k^3} = \frac{1}{4(2\pi)} \int \frac{dk^2 \tanh \frac{k^3}{2T}}{k^3} \\ &= \frac{1}{4(2\pi)(2T)^{1/3}} \int_0^\infty \frac{dx \tanh x^{3/2}}{x^{3/2}} \simeq 0.09T^{-1/3}. \quad (\text{A13}) \end{aligned}$$

For the cubic dispersion without angular dependence, the results again differ by a factor of 3. So, the temperature dependence for cubic dispersion with and without HOVHS is identical.

APPENDIX B: CALCULATION OF POLARIZATION OPERATORS IN THE OVHS LIMIT

In the OVHS limit, $\gamma = 1$ and the dispersion for two patches is identical

$$\varepsilon_{\mathbf{k}}^\pm = k^2 \cos 2\theta = \varepsilon_k,$$

where \pm label valleys (patches). As previously, we will use temperature as a regularizer. In our sign convention the four polarization are given by

$$\begin{aligned} \Pi_{ph}(0) &= \Pi_{ph}(Q) = -T \sum_\omega \int \frac{d^2k}{4\pi^2} \frac{1}{(i\omega - \varepsilon_k)^2} = I_1, \\ \Pi_{pp}(0) &= \Pi_{pp}(Q) = T \sum_\omega \int \frac{d^2k}{4\pi^2} \frac{1}{(i\omega - \varepsilon_k)(-i\omega - \varepsilon_k)} = I_2, \quad (\text{B1}) \end{aligned}$$

where

$$I_1 = \frac{1}{4T} \int \frac{d^2k}{4\pi^2} \frac{1}{\cosh^2 \frac{\varepsilon_k}{2T}}, \quad I_2 = \frac{1}{2} \int \frac{d^2k \tanh \frac{\varepsilon_k}{2T}}{4\pi^2 \varepsilon_k}.$$

For both integrals we need to set the upper limit of integration over k . We set it at $k = 1$. Consider I_1 first. Introducing $\varepsilon_k = k^2 \cos 2\theta$ and $u = \cos 2\theta$ as new variables and integrating over ε_k , we obtain

$$I_1 = \frac{1}{4\pi^2} \int_0^1 \frac{du \tanh \frac{u}{2T}}{u\sqrt{1-u^2}}. \quad (\text{B2})$$

Evaluating the integral, we obtain

$$I_1 = \frac{1}{4\pi^2} \log \frac{2.26}{T}. \quad (\text{B3})$$

Just as in the HOVHS case we can also evaluate the integral approximately by expanding around the angles θ for which $\cos 2\theta = 0$. Doing this, we obtain

$$\begin{aligned} I_1 &= \frac{1}{4T(2\pi)^2} \int \frac{d^2k}{\cosh^2 \frac{\varepsilon_k}{2T}} \simeq \frac{4}{4T(2\pi)^2} \int \frac{kdkd\theta}{\cosh^2 \frac{2k^2\theta}{2T}} \\ &\simeq \int_0^{O(1)} \frac{d\theta}{\theta(2\pi)^2} \int_0^{\theta/T} \frac{d(k^2\theta/T)}{\cosh^2 \frac{k^2\theta}{T}} \\ &= \frac{1}{4\pi^2} \int_0^{O(1)} d\theta \frac{\tanh \theta/T}{\theta} = \frac{1}{4\pi^2} \ln \frac{b}{T}, \quad b = O(1). \quad (\text{B4}) \end{aligned}$$

We see that to logarithmic accuracy, the approximate expression for I_1 coincides with the exact one.

For I_2 , we obtain, by changing the variables in the integrand to $x = 2\theta$ and $y = k^2 \cos 2\theta / (2T)$,

$$I_2 = \frac{1}{4\pi^2} \int_0^{\pi/2} \frac{dx}{x} \int_0^{x/(2T)} dy \frac{\tanh y}{y}. \quad (\text{B5})$$

Evaluating the integral with logarithmic accuracy, we obtain

$$I_2 = \frac{1}{8\pi^2} \log^2 \left(\frac{a}{T} \right), \quad a = O(1). \quad (\text{B6})$$

To logarithmic accuracy, the same expression is obtained if we expand around the angles for which $\cos 2\theta = 0$.

APPENDIX C: CALCULATION OF POLARIZATION OPERATORS CLOSE to the OVHS limit: $\gamma \leq 1$

In this section, we present approximate expressions for the polarization bubbles for γ , which on one hand are close to one, and on the other are such that $\sqrt{1-\gamma^2} > T$.

1. Calculation of $\Pi_{ph}(0)$

The intravalley particle-hole susceptibility is given by

$$\begin{aligned} \Pi_{ph}(0) &= \frac{1}{4T(2\pi)^2} \int \frac{d^2k}{\cosh^2 \frac{\varepsilon_{\mathbf{k}}^+}{2T}} \\ &= \frac{1}{4T(2\pi)^2} \int \frac{d^2k}{\cosh^2 \frac{\gamma k^2 \cos 2\theta + \sqrt{1-\gamma^2} k^3 \cos 3\theta}{2T}}. \end{aligned} \quad (\text{C1})$$

To calculate the integral we expand around $\theta = \pi/4, 3\pi/4, 5\pi/4, 7\pi/4$ since the main contribution comes from the vicinity of these angles. Around these angles,

$$\varepsilon_{\mathbf{k}}^+ \simeq \pm 2\gamma k^2 \theta \pm \frac{\sqrt{1-\gamma^2}}{\sqrt{2}} k^3,$$

Since \cosh is an even function one needs to consider only two angles, the other two will give the same result. Choosing θ near $\pi/4$ and $3\pi/4$, we obtain near these angles

$$\varepsilon_{\mathbf{k}}^+ \simeq 2\gamma k^2 \theta + \frac{\sqrt{1-\gamma^2}}{\sqrt{2}} k^3, \quad (\text{C2})$$

and

$$\varepsilon_{\mathbf{k}}^+ \simeq 2\gamma k^2 \theta - \frac{\sqrt{1-\gamma^2}}{\sqrt{2}} k^3.$$

With this one can approximate the particle-hole susceptibility as

$$\begin{aligned} \Pi_{ph}(0) &\simeq \frac{2}{4T(2\pi)^2} \int \frac{kdkd\theta}{\cosh^2 \frac{2\gamma k^2 \theta + \frac{\sqrt{1-\gamma^2}}{\sqrt{2}} k^3}{2T}} \\ &+ \frac{2}{4T(2\pi)^2} \int \frac{kdkd\theta}{\cosh^2 \frac{2\gamma k^2 \theta - \frac{\sqrt{1-\gamma^2}}{\sqrt{2}} k^3}{2T}}. \end{aligned} \quad (\text{C3})$$

Consider the first of the two integrals,

$$\frac{1}{T} \int \frac{d^2k}{\cosh^2 \frac{2\gamma k^2 \theta + \frac{\sqrt{1-\gamma^2}}{\sqrt{2}} k^3}{2T}}. \quad (\text{C4})$$

It is convenient to introduce new variables,

$$\bar{k} = k \frac{(1-\gamma^2)^{1/6}}{\sqrt{2}T^{1/3}}, \quad \bar{\alpha} = \frac{2\gamma}{(1-\gamma^2)^{1/3}T^{1/3}}.$$

Then, the first integral can be rewritten in the following form:

$$\frac{2}{(1-\gamma^2)^{1/3}T^{1/3}} \int \frac{d^2\bar{k}}{\cosh^2(\bar{\alpha}\bar{k}^2\theta + \bar{k}^3)}. \quad (\text{C5})$$

The scaling function $f(\gamma)$ is given by the integral, where $\bar{\alpha}(\gamma) \gg 1$ for γ slightly smaller than 1. We calculate the integral analytically for $\bar{\alpha} \gg 1$ to logarithmic accuracy. We will first integrate over the angle θ and then integrate over \bar{k} . Let us rewrite the integral (C5),

$$\begin{aligned} &\frac{2}{(1-\gamma^2)^{1/3}T^{1/3}} \int \frac{d^2\bar{k}}{\cosh^2(\bar{\alpha}\bar{k}^2\theta + \bar{k}^3)} \\ &= \frac{2}{(1-\gamma^2)^{1/3}T^{1/3}} \int \frac{\bar{k}d\bar{k}}{\bar{\alpha}\bar{k}^2} \int \frac{d(\bar{\alpha}\bar{k}^2\theta)}{\cosh^2(\bar{\alpha}\bar{k}^2\theta + \bar{k}^3)}. \end{aligned} \quad (\text{C6})$$

For θ the region of integration is $\theta \in [0, 1]$. The cubic terms can be neglected for $\bar{\alpha}\bar{k}^2\theta > \bar{k}^3$. Then, for the integration over $x = \bar{\alpha}\bar{k}^2\theta$, the limit is defined by the condition on the smallness of cubic terms,

$$\bar{\alpha}\theta > \bar{k} \Rightarrow x < \bar{\alpha}\theta \cdot (\bar{\alpha}\theta)^2 = (\bar{\alpha}\theta)^3.$$

For maximal $\theta = 1$ the upper limit for \bar{k} is then just $\bar{\alpha}$. We use those integration boundaries, introduce variable $x = \bar{\alpha}\bar{k}^2\theta + \bar{k}^3$, and obtain

$$\frac{2}{(1-\gamma^2)^{1/3}T^{1/3}} \int_0^{\bar{\alpha}} \frac{\bar{k}d\bar{k}}{\bar{\alpha}\bar{k}^2} \int_{\bar{k}^3}^{\bar{\alpha}\bar{k}^2 + \bar{k}^3} \frac{dx}{\cosh^2 x}. \quad (\text{C7})$$

The first integration is straightforward,

$$\begin{aligned} &\frac{2}{(1-\gamma^2)^{1/3}T^{1/3}} \int_0^{\bar{\alpha}} \frac{\bar{k}d\bar{k}}{\bar{\alpha}\bar{k}^2} \int_{\bar{k}^3}^{\bar{\alpha}\bar{k}^2 + \bar{k}^3} \frac{dx}{\cosh^2 x} \\ &= \frac{2}{(1-\gamma^2)^{1/3}T^{1/3}} \int_0^{\bar{\alpha}} \frac{\bar{k}d\bar{k}}{\bar{\alpha}\bar{k}^2} [\tanh(\bar{\alpha}\bar{k}^2 + \bar{k}^3) - \tanh(\bar{k}^3)]. \end{aligned} \quad (\text{C8})$$

Now let us consider the second integral in (C3). After performing exactly the same transformations (except for the variable x , which now reads $x = \bar{\alpha}\bar{k}^2\theta - \bar{k}^3$, the lower limit of integration over x changes) we get

$$\frac{2}{(1-\gamma^2)^{1/3}T^{1/3}} \int_0^{\bar{\alpha}} \frac{\bar{k}d\bar{k}}{\bar{\alpha}\bar{k}^2} [\tanh(\bar{\alpha}\bar{k}^2 + \bar{k}^3) + \tanh(\bar{k}^3)]. \quad (\text{C9})$$

As one can see now, terms with $\tanh \bar{k}^3$ in (C8) and (C9) cancel each other, so $\Pi_{ph}(0)$ is

$$\Pi_{ph}(0) = \frac{4}{(1-\gamma^2)^{1/3}T^{1/3}8\pi^2} \int_0^{\bar{\alpha}} \frac{\bar{k}d\bar{k}}{\bar{\alpha}\bar{k}^2} \tanh(\bar{\alpha}\bar{k}^2 + \bar{k}^3). \quad (\text{C10})$$

This integral can be evaluated with logarithmic accuracy. Neglecting k^3 under the tanh one gets

$$\begin{aligned}\Pi_{ph}(0) &\simeq \frac{1}{(1-\gamma^2)^{1/3}T^{1/3}2\pi^2} \int_0^{\bar{\alpha}} \frac{\bar{k}d\bar{k}}{\bar{\alpha}\bar{k}^2} \tanh(\bar{\alpha}\bar{k}^2) \\ &= \frac{1}{(1-\gamma^2)^{1/3}T^{1/3}4\pi^2\bar{\alpha}} \int_0^{\bar{\alpha}^3} \frac{dx}{x} \tanh x \\ &\simeq \frac{3}{8\pi^2\gamma} \ln \frac{2\gamma}{T^{1/3}(1-\gamma^2)^{1/3}}.\end{aligned}\quad (C11)$$

Note that one cannot strictly take the limit $\gamma \rightarrow 1$ as we assumed $\sqrt{1-\gamma^2} > T$.

2. Calculation of $\Pi_{ph}(Q)$

The intervalley particle-hole susceptibility is given by

$$\Pi_{ph}(Q) = -T \sum_{\omega} \int \frac{d^2k}{(i\omega - \varepsilon_{\mathbf{k}}^+)(i\omega - \varepsilon_{\mathbf{k}}^-)}, \quad (C12)$$

where $\varepsilon_{\mathbf{k}}^+ = \gamma k^2 \cos 2\theta + \sqrt{1-\gamma^2}k^3 \cos 3\theta$ and $\varepsilon_{\mathbf{k}}^- = \gamma k^2 \cos 2\theta - \sqrt{1-\gamma^2}k^3 \cos 3\theta$. We first sum over Matsubara frequencies and obtain

$$\begin{aligned}\Pi_{ph}(Q) &= -T \sum_{\omega} \int \frac{d^2k}{(i\omega - \varepsilon_{\mathbf{k}}^+)(i\omega - \varepsilon_{\mathbf{k}}^-)} \\ &= -\frac{1}{2(2\pi)^2} \int \frac{d^2k \left(\tanh \frac{\varepsilon_{\mathbf{k}}^-}{2T} - \tanh \frac{\varepsilon_{\mathbf{k}}^+}{2T} \right)}{\varepsilon_{\mathbf{k}}^+ - \varepsilon_{\mathbf{k}}^-} \\ &= -\frac{1}{4(2\pi)^2} \int \frac{kdkd\theta \left(\tanh \frac{\varepsilon_{\mathbf{k}}^-}{2T} - \tanh \frac{\varepsilon_{\mathbf{k}}^+}{2T} \right)}{\sqrt{1-\gamma^2}k^3 \cos 3\theta}.\end{aligned}\quad (C13)$$

We will now expand around $\theta \simeq 3\pi/4$ and proceed with an approximate dispersion. The reason for this approximation is twofold. First, the double-log contribution comes from the k^2 dispersion near the zero energy lines [given by $\theta \simeq (2n+1)\pi/4$]. Second, as we saw above, the cubic term gives the $\sim T^{-1/3}$ dependence regardless of whether there is angular dependence or not. Furthermore, tanh is an odd function, hence, we can again consider only the case near one angle to get the results to logarithmic accuracy [like we did for $\Pi_{ph}(0)$]. Expanding near $\theta \simeq 3\pi/4$ and changing variables

$$\Pi_{pp}(Q) = \frac{1}{2(2\pi)^2} \int \frac{d^2k \left(\tanh \frac{\varepsilon_{\mathbf{k}}^+}{2T} + \tanh \frac{\varepsilon_{\mathbf{k}}^-}{2T} \right)}{\varepsilon_{\mathbf{k}}^+ + \varepsilon_{\mathbf{k}}^-} = \frac{1}{2(2\pi)^2} \int \frac{d^2k \left(\tanh \frac{\gamma k^2 \cos 2\theta + \sqrt{1-\gamma^2}k^3 \cos 3\theta}{2T} + \tanh \frac{\gamma k^2 \cos 2\theta - \sqrt{1-\gamma^2}k^3 \cos 3\theta}{2T} \right)}{2\gamma k^2 \cos 2\theta}, \quad (C17)$$

where we used Eq. (5) and that $\varepsilon_{-\mathbf{k}}^+ = \varepsilon_{\mathbf{k}}^-$.

Since we calculate the integral in the limit of small $\sqrt{1-\gamma^2}$, we can again consider only one case (tanh is an odd function, so every time $\cos 2\theta$ changes sign tanh will change the sign as well and the integral remains positive). We expand around $\theta \simeq 3\pi/4$ (to have $\cos 2\theta$ being positive) and obtain

just like for $\Pi_{ph}(0)$ we get

$$\begin{aligned}\Pi_{ph}(Q) &\simeq - \int \frac{d^2\bar{k} (\tanh(\bar{\alpha}\bar{k}^2\theta - \bar{k}^3) - \tanh(\bar{\alpha}\bar{k}^2\theta + \bar{k}^3))}{\bar{k}^3(1-\gamma^2)^{1/3}T^{1/3}(2\pi)^2} \\ &= - \int \frac{d\bar{k}d\theta (\tanh(\bar{\alpha}\bar{k}^2\theta - \bar{k}^3) - \tanh(\bar{\alpha}\bar{k}^2\theta + \bar{k}^3))}{\bar{k}^2(1-\gamma^2)^{1/3}T^{1/3}(2\pi)^2},\end{aligned}\quad (C14)$$

We are interested in the regime with large $\bar{\alpha} \gg 1$ where quadratic dispersion dominates. This allows us to expand the difference between two hyperbolic tangents in Taylor series using $\bar{k}^3/\bar{\alpha}\bar{k}^2\theta$ as a small parameter. This means that $\bar{k}/\bar{\alpha}\theta < 1$, i.e., $\bar{k} < \bar{\alpha}\theta$. Using this, we evaluate the integral as

$$\begin{aligned}&\int \frac{d\bar{k}d\theta (\tanh(\bar{\alpha}\bar{k}^2\theta - \bar{k}^3) - \tanh(\bar{\alpha}\bar{k}^2\theta + \bar{k}^3))}{\bar{k}^2} \\ &\simeq \int \frac{d\bar{k}d\theta \cdot 2\bar{\alpha}\bar{k}^2\theta (\tanh^2(\bar{\alpha}\bar{k}^2\theta) - 1) \frac{\bar{k}^3}{\bar{\alpha}\bar{k}^2\theta}}{\bar{k}^2} \\ &= \int 2\bar{k}d\bar{k}d\theta \cdot (\tanh^2(\bar{\alpha}\bar{k}^2\theta) - 1) \\ &= - \int_0^{\bar{\alpha}} \frac{2\bar{k}d\bar{k}}{\bar{\alpha}\bar{k}^2} \int_0^1 \frac{d(\bar{\alpha}\bar{k}^2\theta)}{\cosh^2(\bar{\alpha}\bar{k}^2\theta)} \\ &= -2 \int_0^{\bar{\alpha}} \frac{\bar{k}d\bar{k}}{\bar{\alpha}\bar{k}^2} \int_0^{\bar{\alpha}\bar{k}^2} \frac{dx}{\cosh^2 x}.\end{aligned}\quad (C15)$$

Substituting into (C14), we obtain

$$\begin{aligned}\Pi_{ph}(Q) &= \frac{2}{(1-\gamma^2)^{1/3}T^{1/3}(2\pi)^2} \int_0^{\bar{\alpha}} \frac{\bar{k}d\bar{k}}{\bar{\alpha}\bar{k}^2} \tanh \bar{\alpha}\bar{k}^2 \\ &= \frac{1}{(1-\gamma^2)^{1/3}T^{1/3}(2\pi)^2\bar{\alpha}} \int_0^{\bar{\alpha}^3} \frac{dx}{x} \tanh x \\ &\simeq \frac{3}{8\pi^2\gamma} \ln \frac{2\gamma}{T^{1/3}(1-\gamma^2)^{1/3}}.\end{aligned}\quad (C16)$$

We see that $\Pi_{ph}(Q) \approx \Pi_{ph}(0)$ not only at $\gamma = 1$ but also in the intermediate regime $\gamma \leq 1$. This agrees with the numerical results in Fig. 5.

3. Calculation of $\Pi_{pp}(Q)$

Let us now calculate the intravalley particle-particle susceptibility. It is given by

$$\begin{aligned}\Pi_{pp}(Q) &\simeq \frac{4}{2(2\pi)^2} \int \frac{d^2k \cdot 2 \tanh \left(\frac{2\gamma k^2\theta}{2T} \right)}{4\gamma k^2\theta} \\ &= \frac{1}{(2\pi)^2 T} \int \frac{kdkd\theta \cdot \tanh \left(\frac{\gamma k^2\theta}{T} \right)}{\gamma k^2\theta/T}.\end{aligned}\quad (C18)$$

Here we will integrate over momentum after we integrate over the angle. To do so, we first need to define the limits of integration. Integration over θ runs from 0 to 1, i.e., $\theta \in [0, 1]$. The cutoff on k is defined through the condition $\gamma k^2 \theta \sim \sqrt{1 - \gamma^2 k^3}$. For $\theta \sim 1$ the maximal value of k is of the order of $\frac{\gamma}{\sqrt{1 - \gamma^2}}$, hence $k \in [0, \frac{\gamma}{\sqrt{1 - \gamma^2}}]$. The lower cutoff in θ is governed by the condition $\frac{\gamma}{\sqrt{1 - \gamma^2}} k^2 \theta > k^3$. With this, we can now proceed with the integration,

$$\begin{aligned} \Pi_{pp}(Q) &\simeq \frac{1}{(2\pi)^2 T} \int k dk d\theta \cdot \frac{\tanh\left(\frac{\gamma k^2 \theta}{T}\right)}{\gamma k^2 \theta / T} \\ &= \frac{1}{(2\pi)^2} \int_0^{\frac{\gamma}{\sqrt{1 - \gamma^2}}} \frac{k dk}{\gamma k^2} \int_{\frac{k \sqrt{1 - \gamma^2}}{\gamma}}^1 \frac{d(\gamma k^2 \theta / T) \cdot \tanh\left(\frac{\gamma k^2 \theta}{T}\right)}{\gamma k^2 \theta / T} \\ &= \frac{1}{(2\pi)^2} \int_0^{\frac{\gamma}{\sqrt{1 - \gamma^2}}} \frac{k dk}{\gamma k^2} \int_{\frac{\sqrt{1 - \gamma^2} k^3}{T}}^{\gamma k^2 / T} \frac{dx \cdot \tanh x}{x}. \end{aligned} \quad (C19)$$

Let us now take the integral over x to logarithmic accuracy. We obtain

$$\begin{aligned} \Pi_{pp}(Q) &\simeq \frac{1}{(2\pi)^2} \int_0^{\frac{\gamma}{\sqrt{1 - \gamma^2}}} \frac{k dk}{\gamma k^2} \cdot \left[\ln\left(\frac{\gamma k^2}{T}\right) \tanh\left(\frac{\gamma k^2}{T}\right) - \right. \\ &\quad \left. - \ln\left(\frac{\sqrt{1 - \gamma^2} k^3}{T}\right) \tanh\left(\frac{\sqrt{1 - \gamma^2} k^3}{T}\right) \right]. \end{aligned} \quad (C20)$$

Consider the first contribution. Taking the resulting integral over \bar{k} to logarithmic accuracy we get

$$\begin{aligned} &\frac{1}{(2\pi)^2} \int_0^{\frac{\gamma}{\sqrt{1 - \gamma^2}}} \frac{k dk}{\gamma k^2} \ln\left(\frac{\gamma k^2}{T}\right) \tanh\left(\frac{\gamma k^2}{T}\right) \\ &= \frac{1}{2(2\pi)^2 \gamma} \int_0^{\frac{\gamma^3}{(1 - \gamma^2)\gamma}} \frac{dy}{y} \ln y \tanh y \\ &\simeq \frac{9}{4(2\pi)^2 \gamma} \ln^2 \frac{\gamma}{(1 - \gamma^2)^{1/3} T^{1/3}}. \end{aligned} \quad (C21)$$

The second contribution is

$$\begin{aligned} &-\frac{1}{(2\pi)^2} \int_0^{\frac{\gamma}{\sqrt{1 - \gamma^2}}} \frac{k dk}{\gamma k^2} \ln\left(\frac{\sqrt{1 - \gamma^2} k^3}{T}\right) \tanh\left(\frac{\sqrt{1 - \gamma^2} k^3}{T}\right) \\ &= -\frac{1}{3\gamma(2\pi)^2} \int_0^{\frac{\gamma^3}{(1 - \gamma^2)\gamma}} \frac{dy}{y} \ln y \tanh y \simeq \\ &\simeq -\frac{9}{6(2\pi)^2 \gamma} \ln^2 \frac{\gamma}{(1 - \gamma^2)^{1/3} T^{1/3}}. \end{aligned} \quad (C22)$$

The final result for $\Pi_{pp}(Q)$ is then given by

$$\Pi_{pp}(Q) \approx \frac{3}{4(2\pi)^2 \gamma} \ln^2 \frac{\gamma}{(1 - \gamma^2)^{1/3} T^{1/3}}. \quad (C23)$$

4. Calculation of $\Pi_{pp}(0)$

We perform the same calculation for $\Pi_{pp}(0)$. We first calculate the Matsubara sum,

$$\begin{aligned} \Pi_{pp}(0) &= \frac{1}{2(2\pi)^2} \int \frac{d^2 k \tanh \frac{\varepsilon_{\mathbf{k}}^+}{2T}}{\varepsilon_{\mathbf{k}}^+} \\ &= \frac{1}{2(2\pi)^2} \int \frac{d^2 k \tanh \frac{\gamma k^2 \cos 2\theta + \sqrt{1 - \gamma^2} k^3 \cos 3\theta}{2T}}{\gamma k^2 \cos 2\theta + \sqrt{1 - \gamma^2} k^3 \cos 3\theta}, \end{aligned} \quad (C24)$$

where in Eq. (5) we used that $\varepsilon_{\mathbf{k}}^+ = \varepsilon_{-\mathbf{k}}^-$. Let us again work near $\theta = 3\pi/4$. Then, the integral can be rewritten as

$$\Pi_{pp}(0) \simeq \frac{4}{2(2\pi)^2 T^{1/3} (1 - \gamma^2)^{1/3}} \int \frac{d^2 \bar{k} \tanh(\bar{\alpha} \bar{k}^2 \theta + \bar{k}^3)}{\bar{\alpha} \bar{k}^2 \theta + \bar{k}^3} \quad (C25)$$

using the same change of variables

$$\bar{k} = k \frac{(1 - \gamma^2)^{1/6}}{\sqrt{2} T^{1/3}}, \quad \bar{\alpha} = \frac{2\gamma}{(1 - \gamma^2)^{1/3} T^{1/3}}.$$

We again will first integrate over the angle and only then proceed to the \bar{k} integration. The integration limits are: $\theta \in [-\bar{k}/\bar{\alpha}, 1]$ and $\bar{k} \in [0, \bar{\alpha}]$ (the main contribution here comes from very small angles). Hence, the integral is

$$\begin{aligned} \Pi_{pp}(0) &\simeq \frac{4(1 - \gamma^2)^{-1/3}}{2(2\pi)^2 T^{1/3}} \int \frac{\bar{k} d\bar{k} d\theta \cdot \tanh(\bar{\alpha} \bar{k}^2 \theta + \bar{k}^3)}{\bar{\alpha} \bar{k}^2 \theta + \bar{k}^3} \\ &= \frac{4(1 - \gamma^2)^{-1/3}}{2(2\pi)^2 T^{1/3}} \int_0^{\bar{\alpha}} \frac{\bar{k} d\bar{k}}{\bar{\alpha} \bar{k}^2} \int_{-\bar{k}/\bar{\alpha}}^1 \frac{(\bar{\alpha} \bar{k}^2) d\theta \cdot \tanh(\bar{\alpha} \bar{k}^2 \theta + \bar{k}^3)}{\bar{\alpha} \bar{k}^2 \theta + \bar{k}^3} \\ &= \frac{4(1 - \gamma^2)^{-1/3}}{2(2\pi)^2 T^{1/3}} \int_0^{\bar{\alpha}} \frac{\bar{k} d\bar{k}}{\bar{\alpha} \bar{k}^2} \int \frac{d(\bar{\alpha} \bar{k}^2 \theta + \bar{k}^3) \cdot \tanh(\bar{\alpha} \bar{k}^2 \theta + \bar{k}^3)}{\bar{\alpha} \bar{k}^2 \theta + \bar{k}^3} \\ &= \frac{4(1 - \gamma^2)^{-1/3}}{2(2\pi)^2 T^{1/3}} \int_0^{\bar{\alpha}} \frac{\bar{k} d\bar{k}}{\bar{\alpha} \bar{k}^2} \int_0^{\bar{\alpha} \bar{k}^2 + \bar{k}^3} \frac{dx \cdot \tanh x}{x}. \end{aligned} \quad (C26)$$

To logarithmic accuracy, the last integral reads

$$\frac{4(1 - \gamma^2)^{-1/3}}{2(2\pi)^2 T^{1/3}} \int_0^{\bar{\alpha}} \frac{\bar{k} d\bar{k}}{\bar{\alpha} \bar{k}^2} [\ln(\bar{\alpha} \bar{k}^2 + \bar{k}^3) \tanh(\bar{\alpha} \bar{k}^2 + \bar{k}^3)]. \quad (C27)$$

This integral for large $\bar{\alpha}$ is almost exactly the same as in (C21),

$$\frac{4(1 - \gamma^2)^{-1/3}}{2(2\pi)^2 T^{1/3}} \int_0^{\bar{\alpha}} \frac{\bar{k} d\bar{k}}{\bar{\alpha} \bar{k}^2} [\ln(\bar{\alpha} \bar{k}^2) \tanh(\bar{\alpha} \bar{k}^2)]. \quad (C28)$$

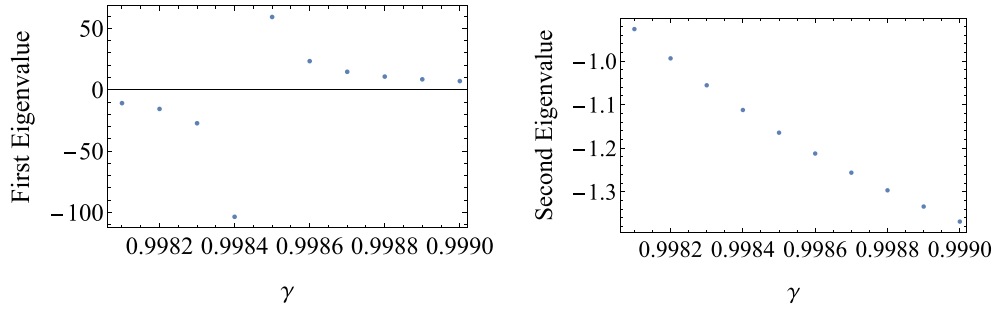


FIG. 11. The two eigenvalues of the pRG flow at the fixed point P_3 in the vicinity of $\gamma_{c1} = 0.9984$, where P_3 approaches $(-\infty, -\infty)$ and then reemerges at (∞, ∞) . One eigenvalue diverges at γ_{c1} and changes sign, the other evolves continuously through γ_{c1} . As a result, a half-stable fixed point on one side of γ_{c1} becomes a stable fixed point on the other side.

We then obtain

$$\Pi_{pp}(0) \approx \frac{9}{4(2\pi)^2\gamma} \ln^2 \frac{2\gamma}{(1-\gamma^2)^{1/3}T^{1/3}}. \quad (\text{C29})$$

Comparing $\Pi_{pp}(Q)$ and $\Pi_{pp}(0)$ we see that the two now differ by a factor of 3. This is different from $\Pi_{pp}(Q) = \Pi_{pp}(0)$ at $\gamma = 1$ (OVHS case). We see therefore that the ratio $\Pi_{pp}(0)/\Pi_{pp}(Q)$ rapidly increases from one to three as γ decreases slightly down from one. This result is in agreement

with the behavior which we found numerically in Fig. 5. Indeed, the ratio $\Pi_{pp}(0)/\Pi_{pp}(Q)$ is close to 3 for all γ in this figure, down to the HOVHS value $\gamma = 0$.

APPENDIX D: FITTING OF THE POLARIZATION BUBBLES

The numerical results for the polarization bubbles for arbitrary γ are shown in Fig. 5. We fitted the numerical results with the scaling functions

$$\begin{aligned} \Pi_{pp}(0) &= 4.05 - 2.81\gamma - 7.4\gamma^2 + 13.8508\gamma^3 - 6.446\gamma^4, \\ \Pi_{ph}(0) &= (0.37 - 0.798\gamma - 0.453\gamma^2 + 4.729\gamma^3 - 6.38\gamma^4 + 2.646\gamma^5)\Pi_{pp}(0), \\ \Pi_{ph}(Q) &= (0.876 - 6.32\gamma + 24.774\gamma^2 - 47.15\gamma^3 + 42.817\gamma^4 - 14.868\gamma^5)\Pi_{pp}(0), \\ \Pi_{pp}(Q) &= \{0.618 + 0.382e^{166.7(\gamma-1)} + 0.213 \tan^{-1}[2.4486(\gamma-1)]\}\Pi_{pp}(0). \end{aligned} \quad (\text{D1})$$

These are not the “exact” expressions, but they fit the numerical results rather well (see Fig. 5). For $\gamma \ll 1$, the results are quite consistent with Eq. (7) in the sense that $\Pi_{pp}(0) \approx \Pi_{ph}(Q) \approx 3\Pi_{pp}(Q) \approx 3\Pi_{ph}(0)$. For $\gamma \rightarrow 1$, $\Pi_{pp}(0)$ and $\Pi_{pp}(Q)$ are the largest, yet because singularities in the OVHS case are logarithmic, larger γ are needed to match the results in Eq. (6).

APPENDIX E: DETAILS OF THE EVOLUTION OF THE FIXED POINTS OF THE pRG FLOW AND THE ORDERING TENDENCIES

In this Appendix, we discuss in some detail the evolution of the phase diagram with γ .

1. The disappearance of the half-stable fixed point, its reemergence, and the disappearance of the Fermi gas region

The changes in the phase diagram begin when the half-stable fixed point P_3 flows towards $-\infty$. We find that P_3 reaches infinity at $\gamma_{c1} \approx 0.9984$. At infinitesimally smaller γ , P_3 reemerges at $(+\infty, +\infty)$. We checked the eigenvalues and found (see Fig. 11) that one of the eigenvalues passes through infinity and changes sign at γ_{c1} , i.e., a half-stable fixed point reemerges as a fully stable fixed point.

We can verify this analytically. The fixed point P_3 moves along the fixed line $x_4 = \zeta x_2$, where $\zeta \approx 1.43$. Substituting this parametrization into Eq. (10) and solving for the eigenvalues λ at large $|x_2|$, we obtain the quadratic equation

$$\begin{aligned} \lambda^2 + 2x_2(-2 + 2d_{ph}(\mathbf{Q}) + 3d_{ph}(0)\zeta + d_{pp}(\mathbf{Q})\zeta)\lambda \\ + 4x_2^2[(d_{ph}(\mathbf{Q}) - 1)(d_{ph}(\mathbf{Q}) + d_{pp}(\mathbf{Q})\zeta - 1) + d_{ph}(0) \\ \times \zeta(d_{ph}(\mathbf{Q}) + 2d_{pp}(\mathbf{Q})\zeta - 1) + 2d_{ph}(0)^2(\zeta^2 - 2)] = 0, \end{aligned} \quad (\text{E1})$$

which yields

$$\lambda = ax_2 \pm \sqrt{b^2x_2^2} = \begin{cases} (a \pm b)x_2 & \text{if } x_2 > 0 \\ (a \mp b)x_2 & \text{if } x_2 < 0, \end{cases} \quad (\text{E2})$$

where

$$\begin{aligned} a &= 2 - 2d_{ph}(\mathbf{Q}) - 3d_{ph}(0)\zeta - d_{pp}(\mathbf{Q})\zeta \\ b &= [16d_{ph}(0)^2 + 8d_{ph}(0)(d_{ph}(\mathbf{Q}) - 1)\zeta \\ &\quad + (d_{ph}(0) - d_{pp}(\mathbf{Q}))^2\zeta^2]^{1/2}. \end{aligned} \quad (\text{E3})$$

The sign of $a - b$ determines whether the two eigenvalues are of the same or different sign. We plot a and b in Fig. 12. We see that $a - b$ indeed changes the sign at γ_{c1} .

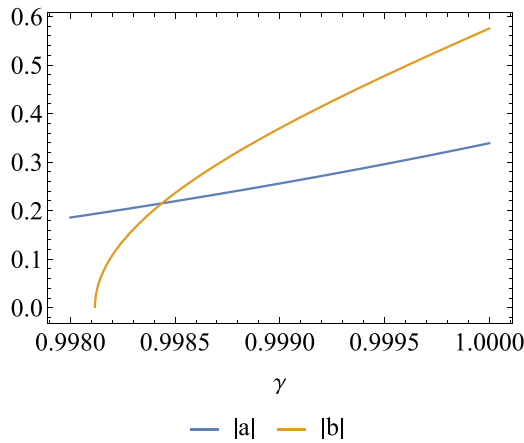


FIG. 12. The parameters a (blue) and b (orange), determined by Eq. (E2). The sign of $a - b$ determines whether the two eigenvalues are of the same or different sign. We see that $a - b$ changes sign at γ_{c1} .

The next event is the annihilation of the half-stable fixed point P_4 and the stable fixed point P_3 at $\gamma_{c2} \approx 0.997$. Naively, one would expect that the annihilation of fixed points resembles the annihilation of two charges with opposite signs in classical electrostatics: the RG flow trajectories follow the same pattern as the field lines between the two charges, which form a dipole. Here the situation is different, however, as the object with a finite charge merges with an object with zero charge. To visualize how the local RG flow changes in response to this anomalous merging process, we draw the schematic diagram in Fig. 13. When the two points merge, the flow across the merging point is in 3-in/1-out, i.e., this point is an inflection point along one direction (the corresponding eigenvalue is zero) and a minimum along the other. At an infinitesimally smaller γ , there is no local extremum, resulting in a continuous flow. In algebraic terms, when the two points merge, the solution of Eq. (9) changes from four distinct real solutions to two degenerate and two nondegenerate solutions. At a smaller γ , two degenerate roots split and become complex, indicating that a fixed point vanishes.

2. The disappearance of the fixed point P_1 and the replacement of the PDW by VP

The behavior of the fixed point P_1 resembles that of P_3 . As γ decreases towards $\gamma_{c3} \approx 0.14$, it gradually moves towards $(-\infty, -\infty)$. At γ infinitesimally smaller than γ_{c3} , P_1 reemerges at $(+\infty, +\infty)$ as a half-stable fixed point (one of the eigenvalues changes the sign). This half-stable fixed point remains on the phase diagram for smaller γ .

Even before P_1 disappears and re-appears, the PDW region on the phase diagram is replaced by VP. One can straightforwardly check that λ_{VP} becomes larger than λ_{PDW} when

$$\frac{2d_{ph}(0)}{d_{pp}(\mathbf{Q}) - d_{ph}(0)} > \frac{|g_4|}{g_2}. \tag{E4}$$

We plot both sides of this equation in Fig. 14. We see that they cross at $\gamma \approx 0.21$. To verify that at γ smaller than this value the ordering tendency changes to VP, we plot in Fig. 15 the eigenvalues in different channels for proper x_2 and x_4 at

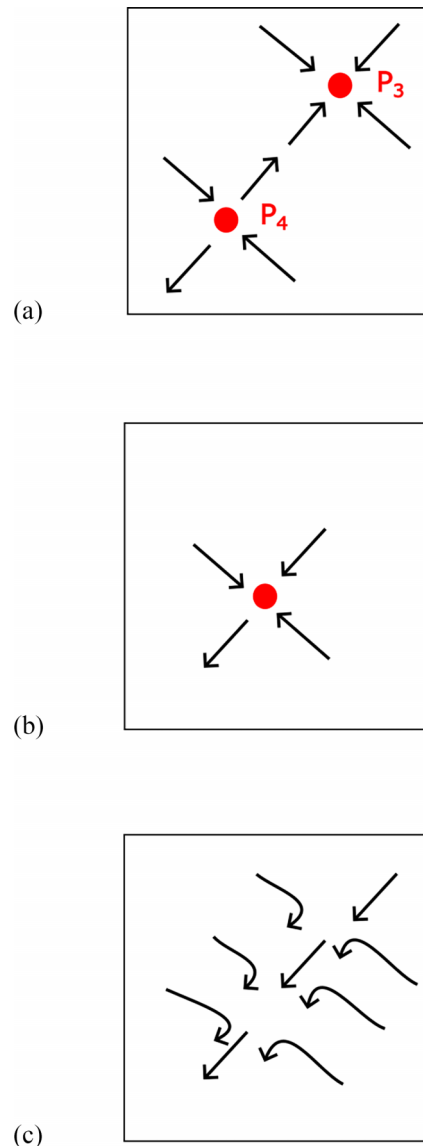


FIG. 13. A schematic picture of how the half-stable fixed point P_4 and the stable fixed point P_3 merge. (a) The two points are close to each other. (b) The moment when they merge. (c) The continuous flow after annihilation.

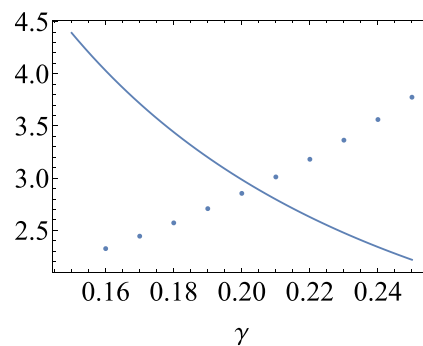


FIG. 14. Graphical visualization of the criterion, Eq. (E4), that determines whether VP or PDW is the leading instability in the bottom right corner of the phase diagram. Solid and dashed lines are left-hand and right-hand sides of Eq. (E4). The two functions cross at $\gamma \approx 0.21$. At smaller γ , VP wins over PDW.

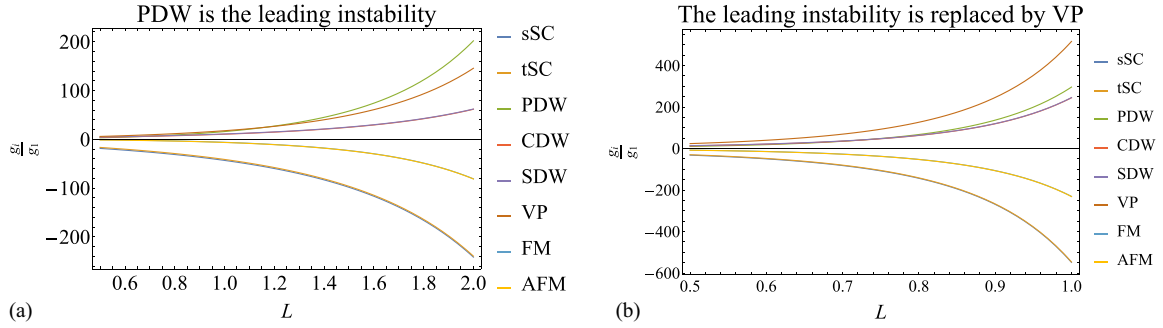


FIG. 15. The flow of the ratios of couplings with the pRG parameter L for bare values $x_2^0 = 5, x_4^0 = 0.1$, which are in the range where the leading ordering tendency at $\gamma = 1$ is PDW. We argued (see the text) that the ordering tendency changes to VP at $\gamma \approx 0.21$. We plot the eigenvalues in different channels for somewhat larger and somewhat smaller γ . For larger $\gamma = 0.22$, PDW is the leading instability; for smaller $\gamma = 0.19$, the leading ordering tendency is VP.

somewhat larger and somewhat smaller γ . For larger $\gamma = 0.22$, PDW is the leading instability; for smaller $\gamma = 0.19$, the leading ordering tendency is VP.

Next, we show that as P_1 disappears and then re-emerges, spin-triplet SC becomes degenerate with spin-singlet SC. We demonstrate this in Fig. 16, where we plot the eigenvalues in different channels for proper x_2 and x_4 . We see that indeed tSC becomes degenerate with sSC once the fixed point P_1 disappears from the lower part of the phase diagram.

3. Pair production of the FM and half-stable fixed point

The final element of the evolution of the pRG flow is the creation of a pair of fixed points P_5 and P_6 in the second quadrant of the phase diagram at $\gamma_{c4} \approx 0.09$. The creation mechanism is exactly opposite to the annihilation of P_3 and P_4 . Still, like there, one of the fixed points is stable (P_6) and

one is half-stable (P_5). In our analytic study we find that at $\gamma > \gamma_{c4}$, there are two complex solutions and two real solutions of Eq. (9). Right at $\gamma = \gamma_{c4}$, the two formerly complex solutions become a degenerate real solution, and at $\gamma < \gamma_{c4}$ they split into two real solutions, i.e., as γ becomes smaller than γ_{c4} , the total number of real solutions changes from 2 to 4. We analyzed the leading ordering tendency in the basin of attraction of the stable fixed point P_6 and found that it is towards global ferromagnetism. At the same line, the phase boundary that starts at the unstable fixed point P_2 and passes through P_5 separates FM and tSC/sSC orders. The RG flow along the phase boundary is also somewhat nontrivial. At $\gamma > \gamma_{c5} \approx 0.04$, the functions $f_i(c_2, c_4)$ in Eq. (11), where c_2 and c_4 are x_2 and x_4 at P_5 , are positive, i.e., the couplings diverge under pRG (the leading instability is tSC). At $\gamma = \gamma_{c5}$, $f_i(c_2, c_4) = 0$, i.e., the couplings remain invariant under pRG, similar to super-metal behavior, reported in [43]. At $\gamma < \gamma_{c5}$, $f_i(c_2, c_4) < 0$, and the couplings tend to zero.

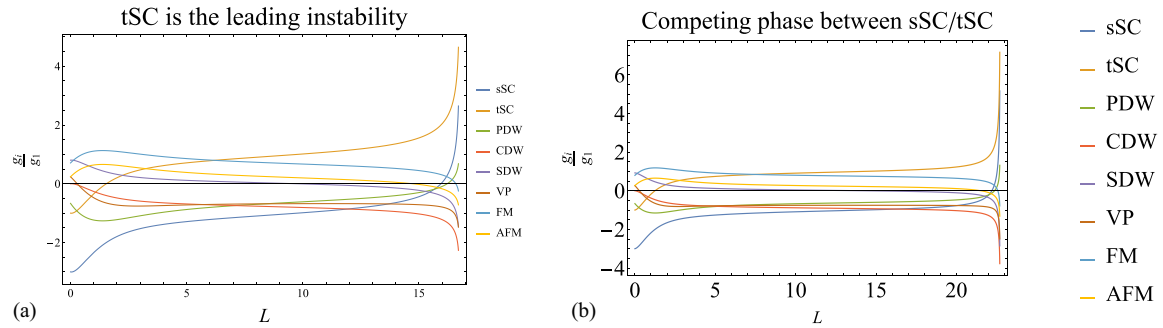


FIG. 16. The flow of the ratios of the coupling as a function of L before ($\gamma = 0.18$) and after the disappearance of the stable fixed point P_1 ($\gamma = 0.12$) using the bare value $x_2^0 = x_4^0 = 2$. One can see that tSC wins over sSC when P_1 is present, but the two are degenerate when P_1 disappears.

[1] B. Keimer, S. A. Kivelson, M. R. Norman, S. Uchida, and J. Zaanen, *Nature (London)* **518**, 179 (2015).
 [2] R. M. Fernandes and A. V. Chubukov, *Rep. Prog. Phys.* **80**, 014503 (2017).
 [3] C. M. Varma, *Rev. Mod. Phys.* **92**, 031001 (2020).

[4] Y. Cao, V. Fatemi, S. Fang, K. Watanabe, T. Taniguchi, E. Kaxiras, and P. Jarillo-Herrero, *Nature (London)* **556**, 43 (2018).
 [5] Y. Cao, V. Fatemi, A. Demir, S. Fang, S. L. Tomarken, J. Y. Luo, J. D. Sanchez-Yamagishi, K. Watanabe, T.

- Taniguchi, E. Kaxiras *et al.*, *Nature (London)* **556**, 80 (2018).
- [6] Y. Cao, D. Rodan-Legrain, J. M. Park, N. F. Q. Yuan, K. Watanabe, T. Taniguchi, R. M. Fernandes, L. Fu, and P. Jarillo-Herrero, *Science* **372**, 264 (2021).
- [7] U. Zondiner, A. Rozen, D. Rodan-Legrain, Y. Cao, R. Queiroz, T. Taniguchi, K. Watanabe, Y. Oreg, F. von Oppen, A. Stern *et al.*, *Nature (London)* **582**, 203 (2020).
- [8] D. Wong, K. P. Nuckolls, M. Oh, B. Lian, Y. Xie, S. Jeon, K. Watanabe, T. Taniguchi, B. A. Bernevig, and A. Yazdani, *Nature (London)* **582**, 198 (2020).
- [9] S. Wu, Z. Zhang, K. Watanabe, T. Taniguchi, and E. Y. Andrei, *Nat. Mater.* **20**, 488 (2021).
- [10] R. Polski, Y. Zhang, Y. Peng, H. S. Arora, Y. Choi, H. Kim, K. Watanabe, T. Taniguchi, G. Refael, F. von Oppen, and S. Nadj-Perge, *arXiv:2205.05225*.
- [11] H. Zhou, L. Holleis, Y. Saito, L. Cohen, W. Huynh, C. L. Patterson, F. Yang, T. Taniguchi, K. Watanabe, and A. F. Young, *Science* **375**, 774 (2022).
- [12] L. Holleis, C. L. Patterson, Y. Zhang, H. M. Yoo, H. Zhou, T. Taniguchi, K. Watanabe, S. Nadj-Perge, and A. F. Young, *arXiv:2303.00742*.
- [13] H. Zhou, T. Xie, T. Taniguchi, K. Watanabe, and A. F. Young, *Nature (London)* **598**, 434 (2021).
- [14] H. Zhou, T. Xie, A. Ghazaryan, T. Holder, J. R. Ehrets, E. M. Spanton, T. Taniguchi, K. Watanabe, E. Berg, M. Serbyn, and A. F. Young, *Nature (London)* **598**, 429 (2021).
- [15] J. M. Park, Y. Cao, K. Watanabe, T. Taniguchi, and P. Jarillo-Herrero, *Nature (London)* **590**, 249 (2021).
- [16] S. Jiang, D. J. Scalapino, and S. R. White, *Proc. Natl. Acad. Sci. USA* **118**, e2109978118 (2021).
- [17] F. Xie, N. Regnault, D. Călugăru, B. A. Bernevig, and B. Lian, *Phys. Rev. B* **104**, 115167 (2021).
- [18] A. V. Chubukov, D. V. Efremov, and I. Eremin, *Phys. Rev. B* **78**, 134512 (2008).
- [19] A. V. Chubukov, M. Khodas, and R. M. Fernandes, *Phys. Rev. X* **6**, 041045 (2016).
- [20] L. Classen, R.-Q. Xing, M. Khodas, and A. V. Chubukov, *Phys. Rev. Lett.* **118**, 037001 (2017).
- [21] M. A. Metlitski and S. Sachdev, *Phys. Rev. B* **82**, 075128 (2010).
- [22] M. A. Metlitski and S. Sachdev, *New J. Phys.* **12**, 105007 (2010).
- [23] S. Sachdev, M. A. Metlitski, and M. Punk, *J. Phys.: Condens. Matter* **24**, 294205 (2012).
- [24] Y. Wang and A. Chubukov, *Phys. Rev. B* **90**, 035149 (2014).
- [25] I. Dzyaloshinskii, *Zh. Eksp. Teor. Fiz.* **93**, 1487 (1987).
- [26] H. J. Schulz, *Europhys. Lett.* **4**, 609 (1987).
- [27] A. Chubukov, *Physica C* **469**, 640 (2009).
- [28] R. Shankar, *Rev. Mod. Phys.* **66**, 129 (1994).
- [29] K. L. Hur and T. Maurice Rice, *Ann. Phys.* **324**, 1452 (2009).
- [30] W. Metzner, M. Salmhofer, C. Honerkamp, V. Meden, and K. Schönhammer, *Rev. Mod. Phys.* **84**, 299 (2012).
- [31] W. Qin, C. Huang, T. Wolf, N. Wei, I. Blinov, and A. H. MacDonald, *Phys. Rev. Lett.* **130**, 146001 (2023).
- [32] N. Furukawa, T. M. Rice, and M. Salmhofer, *Phys. Rev. Lett.* **81**, 3195 (1998).
- [33] R. Nandkishore, L. S. Levitov, and A. V. Chubukov, *Nat. Phys.* **8**, 158 (2012).
- [34] F. Yang, F. Wang, and D.-H. Lee, *Phys. Rev. B* **88**, 100504(R) (2013).
- [35] H. Isobe, N. F. Q. Yuan, and L. Fu, *Phys. Rev. X* **8**, 041041 (2018).
- [36] Y. Sherkunov and J. J. Betouras, *Phys. Rev. B* **98**, 205151 (2018).
- [37] Y.-Z. You and A. Vishwanath, *Phys. Rev. B* **105**, 134524 (2022).
- [38] R. Nandkishore, R. Thomale, and A. V. Chubukov, *Phys. Rev. B* **89**, 144501 (2014).
- [39] L. Van Hove, *Phys. Rev.* **89**, 1189 (1953).
- [40] A. Shtyk, G. Goldstein, and C. Chamon, *Phys. Rev. B* **95**, 035137 (2017).
- [41] N. F. Q. Yuan, H. Isobe, and L. Fu, *Nat. Commun.* **10**, 5769 (2019).
- [42] L. Classen, A. V. Chubukov, C. Honerkamp, and M. M. Scherer, *Phys. Rev. B* **102**, 125141 (2020).
- [43] H. Isobe and L. Fu, *Phys. Rev. Res.* **1**, 033206 (2019).
- [44] S. Link, S. Forti, A. Stöhr, K. Küster, M. Rösner, D. Hirschmeier, C. Chen, J. Avila, M. C. Asensio, A. A. Zakharov, T. O. Wehling, A. I. Lichtenstein, M. I. Katsnelson, and U. Starke, *Phys. Rev. B* **100**, 121407(R) (2019).
- [45] P. Castro, D. Shaffer, Y.-M. Wu, and L. H. Santos, *Phys. Rev. Lett.* **131**, 026601 (2023).
- [46] H. Pan, F. Wu, and S. Das Sarma, *Phys. Rev. Res.* **2**, 033087 (2020).
- [47] Y.-T. Hsu, F. Wu, and S. Das Sarma, *Phys. Rev. B* **104**, 195134 (2021).
- [48] J. Zang, J. Wang, J. Cano, and A. J. Millis, *Phys. Rev. B* **104**, 075150 (2021).
- [49] A. L. Szabó and B. Roy, *Phys. Rev. B* **105**, L201107 (2022).
- [50] Z. Dong, A. V. Chubukov, and L. Levitov, *Phys. Rev. B* **107**, 174512 (2023); Z. Dong, L. Levitov, and A. V. Chubukov, *ibid.* **108**, 134503 (2023).
- [51] D. V. Chichinadze, L. Classen, Y. Wang, and A. V. Chubukov, *Phys. Rev. Lett.* **128**, 227601 (2022).
- [52] D. V. Chichinadze, L. Classen, Y. Wang, and A. V. Chubukov, *npj Quantum Mater.* **7**, 114 (2022).
- [53] J. M. Murray and O. Vafek, *Phys. Rev. B* **89**, 201110(R) (2014).
- [54] R.-Q. Xing, L. Classen, M. Khodas, and A. V. Chubukov, *Phys. Rev. B* **95**, 085108 (2017).
- [55] D. V. Chichinadze, L. Classen, and A. V. Chubukov, *Phys. Rev. B* **102**, 125120 (2020).
- [56] Y.-T. Hsu, F. Wu, and S. Das Sarma, *Phys. Rev. B* **102**, 085103 (2020).
- [57] Y.-P. Lin and R. M. Nandkishore, *Phys. Rev. B* **100**, 085136 (2019).
- [58] Y.-P. Lin and R. M. Nandkishore, *Phys. Rev. B* **102**, 245122 (2020).
- [59] D.-C. Lu, T. Wang, S. Chatterjee, and Y.-Z. You, *Phys. Rev. B* **106**, 155115 (2022).
- [60] L. Klebl, A. Fischer, L. Classen, M. M. Scherer, and D. M. Kennes, *Phys. Rev. Res.* **5**, L012034 (2023).
- [61] L. Wang, E.-M. Shih, A. Ghiotto, L. Xian, D. A. Rhodes, C. Tan, M. Claassen, D. M. Kennes, Y. Bai, B. Kim *et al.*, *Nat. Mater.* **19**, 861 (2020).